

Star formation around the mid-infrared bubble CN 148

L. K. Dewangan^{1*}, D. K. Ojha^{2†}, J. M. C. Grave^{1,3‡}, & K. K. Mallick^{2§}

¹*Centro de Astrofísica, Universidade do Porto, Rua das Estrelas, 4150-762 s/n Porto, Portugal.*

²*Department of Astronomy and Astrophysics, Tata Institute of Fundamental Research, Homi Bhabha Road, Mumbai 400 005, India.*

³*FCNET, Universidade Lusófona do Porto, Rua Augusto Rosa 24, 4000-098, Porto, Portugal*

ABSTRACT

We present a multi-wavelength study to analyse the star formation process associated with the mid-infrared bubble CN 148 (H II region G10.3-0.1), which harbors an O5V-O6V star. The arc-shaped distribution of molecular CO(2-1) emission, the cold dust emission, and the polycyclic aromatic hydrocarbon features trace a photodissociation region (PDR) around the H II region. We have identified 371 young stellar objects (YSOs) in the selected region and, interestingly, their spatial distribution correlates well with the PDR. 41% of these YSOs are present in 13 clusters, each having visual extinction larger than 16 mag. The clusters at the edges of the bubble (both northeast and southwest) are found to be relatively younger than the clusters located further away from the bubble. We also find that four 6.7 GHz methanol masers, two Extended Green Objects, an ultra-compact H II region, and a massive protostar candidate (as previously reported) are spatially positioned at the edges of the bubble. The existence of an apparent age gradient in YSO clusters and different early evolutionary stages of massive star formation around the bubble suggest their origin to be influenced by an H II region expanding into the surrounding interstellar medium. The data sets are suggestive of triggered star formation.

Key words: dust, extinction – H II regions – ISM: bubbles – ISM: individual objects (IRAS 18060-2005) – stars: formation – stars: pre-main sequence

1 INTRODUCTION

The mid-infrared (MIR) bubble, CN 148 (Churchwell et al. 2007) is part of an extended radio H II region, G10.3-0.1 (spatial extent $\sim 12'.8 \times 4'.6$; Kim & Koo 2001), and contains the IRAS 18060-2005 source. The H II region is thought to be associated with the larger W31 molecular cloud complex (e.g., Reich et al. 1990). The W31 complex is comprised of two extended H II regions, G10.2-0.3 and G10.3-0.1 (see Figure 1). The G10.3-0.1 region is estimated to have a far-infrared (FIR) luminosity of about $10^5 L_{\odot}$ (Ghosh et al. 1989; Wood & Churchwell 1989). The object CN 148 was classified as a complete or a closed-ring with an average radius (diameter) and thickness of $1'.41$ ($2'.82$) and $0'.65$ (Churchwell et al. 2007), respectively. The MIR bubble gains its importance due to two embedded sources, “18060nr1733” and “18060nr2481”, which were classified as O5V-O6V and O8V-B2.5V spectral type objects, respectively, based on near-infrared (NIR) K -band spectra (Bik et al. 2005). Bik et al. (2005) also found direct spectroscopic signatures of

strong winds, associated with O5-O6 stars, to be present in the “18060nr1733” K -band spectra. The H II region G10.3-0.1 has been included in numerous studies of the larger W31 complex, carried out at multiple wavelengths (Becker et al. 1994; Brand et al. 1994; Walsh et al. 1998; Kim & Koo 2001, 2002; Beuther et al. 2011). The 21 cm radio continuum emission (spatial resolution $\sim 37'' \times 25''$; from Kim & Koo 2001) revealed an extended bipolar morphology for the G10.3-0.1 region, using the Very Large Array (VLA) DnC-array. Kim & Koo (2001) also reported an ultra-compact (UC) H II region G10.30-0.15 and another compact component surrounded by extended bipolar ionized envelopes. The 21 cm flux was also used to classify the ionizing source as an O4.5 star, assuming a distance of 6.0 kpc. Kim & Koo (2002) suggested the champagne flow model to explain the bipolar radio morphology, using the molecular CO and CS line observations (at $60''$ resolution). These authors found a very high ^{12}CO $J = 2-1/J = 1-0$ intensity ratio (average value ~ 1.4) around the bubble (referred to as a “hollow” in their paper), which led them to suggest ongoing massive star formation (MSF) around the H II region. Using the champagne model, Kim & Koo (2002) estimated the dynamical age of ~ 1.2 Myr for the H II region G10.3-0.1. They concluded that the H II region and its ionizing star is inter-

* Lokesh.Dewangan@astro.up.pt

† ojha@tifr.res.in

‡ jgrave@astro.up.pt

§ kshitiz@tifr.res.in

acting with the surrounding ambient material. Subsequent radio observations at a higher spatial resolution, mapping of the $^{13}\text{CO}(2-1)$ and $\text{C}^{18}\text{O}(2-1)$ emission (resolution $\sim 27''.5$), and the detection of $870\ \mu\text{m}$ APEX ATLASGAL (Schuller et al. 2009) dust continuum emission in this region, revealed several high-mass clumps (Beuther et al. 2011). Beuther et al. (2011) reported three different evolutionary stages of star formation, mainly around the central part of the bipolar nebula in G10.30-0.1. These authors also argued that a triggered star formation process may be responsible for the different evolutionary stages in this region.

Apart from the above characteristics, G10.30-0.1 is known to be associated with several masers and Extended Green Objects (EGOs). Three 6 cm (5 GHz) VLA radio detections (Becker et al. 1994), one water maser (Brand et al. 1994), and four 6.7 GHz Class II methanol masers (Walsh et al. 1998) were reported in this region. Two GLIMPSE EGOs (Cyganowski et al. 2008) were also observed in the north-east (G10.34-0.14) and southwest (G10.29-0.13) directions and both these EGOs are associated with 6.7 GHz Class II as well as 44 GHz Class I methanol masers. The EGOs are thought to be massive YSOs (MYSOs), still undergoing the accretion phase (Cyganowski et al. 2009). Different values of the distance (2.2 kpc, 3.4 kpc, 6.0 kpc, and 14.5 kpc) to G10.3-0.1 are found in the literature (e.g. Wilson 1974; Downes et al. 1980; Corbel et al. 1997; Kim & Koo 2001, 2002; Bik et al. 2005; Cyganowski et al. 2009; Moisés et al. 2011; Beuther et al. 2011; Wienen et al. 2012). Bik et al. (2005) estimated the kinematic distances of the two sources ("18060nr1733" and "18060nr2481") in the range 2.1 (near) - 14.6 (far) kpc, using the CS molecular line radial velocities combined with a Galactic rotation model, while Moisés et al. (2011) estimated an average K -band spectrophotometric distance of ~ 2.39 kpc. The velocities of the molecular gas ($10\text{--}15\ \text{km s}^{-1}$; Kim & Koo 2002), the ionized gas ($8\text{--}12\ \text{km s}^{-1}$; Downes et al. 1980; Kim & Koo 2001), four 6.7 GHz methanol masers ($13\text{--}20\ \text{km s}^{-1}$; Walsh et al. 1998), and two EGOs ($12.7\text{--}13.6\ \text{km s}^{-1}$; Cyganowski et al. 2009) suggest that they are part of the same star-forming region. Wienen et al. (2012) reported observations of three ammonia (NH_3) inversion transitions and estimated the radial velocities of the NH_3 gas between 11.3 and $14.5\ \text{km s}^{-1}$. Cyganowski et al. (2009) and Wienen et al. (2012) reported the near kinematic distance as 1.9 kpc and 2.2 kpc, respectively. Considering the fact that the ionizing candidates, methanol masers, and EGOs are physically associated with the G10.3-0.1 region, the distance of 2.2 kpc is consistent. The spectral type estimated from the 21 cm flux at a distance of 2.2 kpc is also in agreement with the spectral type determined using the K -band spectra for the sources (see Section 3.1.3 in this paper). Therefore, we have chosen a distance of 2.2 kpc for the bubble CN 148 and have adopted this value throughout the present work. Considering the near kinematic distance range (1.9–2.5 kpc; Bik et al. 2005; Cyganowski et al. 2009; Wienen et al. 2012), we anticipate the resulting uncertainty in the chosen distance to be $\sim 15\%$ (i.e., 0.3 kpc).

All these studies clearly indicate the presence of ongoing star formation and of massive stars in a very early evolutionary stage. Previous studies also demonstrate the influence of the H II region on the surrounding interstellar medium (ISM). These multiple signposts of star formation as well as the interesting characteristics of the region have

motivated a further investigation of CN 148. To this end, we revisited the source using *Spitzer* Infrared Array Camera (IRAC; Fazio et al. 2004) data in conjunction with unpublished high sensitivity UKIRT NIR data, a narrow-band H_2 $v=1-0\ \text{S}(1)$ $2.12\ \mu\text{m}$ image, and a radio continuum map at 20 cm of the wider area around the bubble. While systematically taking care of all possible contaminants, we have studied the embedded young stellar populations, their relative distribution with respect to the molecular and ionized gas, cold dust, and polycyclic aromatic hydrocarbon (PAH) emission.

A variety of infrared (IR) and radio (archival and literature) data used for this purpose are described, along with the analysis methods, in Section 2. In Section 3, we present the results of the combined analysis. The possible star formation scenario is discussed in Section 4. The main conclusions are summarized in Section 5.

2 DATA AND ANALYSIS

To study the embedded populations as well as the ongoing star formation process in the target region, we used NIR and MIR surveys. The size of the selected field is $\sim 12'.4 \times 9'.9$, centered at $\alpha_{2000} = 18^{\text{h}}08^{\text{m}}53^{\text{s}}$, $\delta_{2000} = -22^{\circ}05'08''$.

NIR *JHK* images and the point source catalog were obtained from the UKIDSS 6th archival data release (UKIDSSDR6plus) of the Galactic Plane Survey (GPS) (Lawrence et al. 2007). UKIDSS observations were made using the UKIRT Wide Field Camera (WFCAM; Casali et al. 2007) and fluxes were calibrated using the Two Micron All Sky Survey data (2MASS; Skrutskie et al. 2006). WFCAM is an array of four 2048×2048 pixels Rockwell Hawaii-II arrays with a pixel size of $0''.4$. The details of basic data reduction and calibration procedures are described in Dye et al. (2006) and Hodgkin et al. (2009), respectively. Only reliable NIR sources were extracted from the publicly access catalog, following the recommendations from Lucas et al. (2008). Sources visible in all the three NIR (*JHK*) bands and those visible only in the *H* and *K* bands were separately extracted for our selected region. The adopted criteria allowed for the removal of saturated sources, non-stellar sources, and unreliable sources near the sensitivity limits. Magnitudes of saturated bright sources were obtained from 2MASS and appended to the resulting catalogs. Only those sources with magnitude error of 0.1 or less in each band were selected for the study to ensure good photometric quality. As a result, 7864 sources were obtained, which were common to all the three (*J*, *H*, and *K*) bands. Additionally 4710 sources were found in the *H* and *K* bands, without a *J* counterpart.

IR data from the *Spitzer* IRAC ch1 ($3.6\ \mu\text{m}$), ch2 ($4.5\ \mu\text{m}$), ch3 ($5.8\ \mu\text{m}$), and ch4 ($8.0\ \mu\text{m}$) bands were obtained from the GLIMPSE survey (Benjamin et al. 2003; Churchwell et al. 2009), while the Multiband Imaging Photometer for *Spitzer* (MIPS) image at $24\ \mu\text{m}$ was obtained from the MIPS Inner Galactic Plane Survey (MIPSGAL; Carey et al. 2005). Photometry was extracted from the GLIMPSE-I Spring '07 highly reliable Point-Source Catalog. Some sources are well detected in the images but do not have photometric magnitudes in the GLIMPSE-I catalog. We obtained aperture photometry for such sources using the GLIMPSE images at a plate scale of $0''.6/\text{pixel}$. The pho-

tometry was done using a $2''.4$ aperture radius and a sky annulus from $2''.4$ to $7''.3$ in IRAF¹. Apparent magnitudes were calibrated using the IRAC zero-magnitude flux densities, including aperture corrections listed in the IRAC Instrument Handbook-Ver-1.0 (also see Dewangan et al. 2012, 2013). The aperture photometry was also performed on the MIPS GAL 24 μm image using a $7''$ aperture radius and a sky annulus from $7''$ to $13''$ in IRAF. MIPS zero-magnitude flux density, including aperture correction was taken from the MIPS Instrument Handbook-Ver-3.

To examine the shock excited molecular hydrogen (H_2) in the region, we used a narrow-band H_2 $v=1-0$ S(1) 2.12 μm image. The $v=1-0$ S(1) line of H_2 at 2.12 μm is considered as an excellent tracer of shocked regions. A continuum-subtracted narrow-band H_2 image was retrieved from the UKIRT Wide-field Infrared Survey for H_2 (UWISH2) database (Froebrich et al. 2011). The UWISH2 is an unbiased survey of the inner Galactic plane in the H_2 1-0 S(1) line at 2.122 μm ($\Delta\lambda = 0.021 \mu\text{m}$; a velocity resolution of about 2970 km s^{-1}) using WFCAM at UKIRT.

To trace cold and dense region, we used dust continuum FIR and sub-millimeter emission maps. The continuum maps were obtained at 70 μm , 160 μm , 250 μm , 350 μm , and 500 μm as part of the *Herschel* Infrared Galactic Plane Survey (Hi-GAL, Molinari et al. 2010). The angular resolutions (beam FWHM) of these bands are $5''.8$, $12''$, $18''$, $25''$, and $37''$, respectively. We downloaded the processed “Standalone Browse Products”, using the *Herschel* Interactive Processing Environment (HIPE, Ott 2010). The aperture photometry for point sources was carried out in each of the *Herschel* maps using the Graphical Astronomy and Image Analysis (GAIA) tool. The radius of the circular apertures was $12''$, $22''$, $22''$, $30''$, and $42''$ at 70, 160, 250, 350, and 500 μm maps, respectively. The background was estimated in a sky annulus from $20''$ to $30''$ and from $30''$ to $40''$ at 70 and 160 μm , respectively, and in a sky annulus from $60''$ to $90''$ at 250, 350, and 500 μm . Aperture corrections were applied to the total fluxes in each *Herschel* band, which were taken from the *Herschel* Handbooks, available from the *Herschel* Science Centre website². The sub-millimeter continuum map at 870 μm (beam size $\sim 19''.2$) was also retrieved from the ATLASGAL archival survey³.

In order to trace the ionized gas in the region, we used a radio continuum map at 20 cm, which we retrieved from the VLA Multi-Array Galactic Plane Imaging Survey (MAGPIS; Helfand et al. 2006) archive. These observations were carried out with the VLA configurations: B, C, and D. To correct for missing flux on large angular scales, Effelsberg 100-m data were combined with the VLA images. Final processed images were made available with a $6''.2 \times 5''.4$ restoring beam and a pixel scale of $2''/\text{pixel}$.

The observed positions of the 6 cm detections (Becker et al. 1994), EGOs (Cyganowski et al. 2008), ATLASGAL clumps (Contreras et al. 2013), 6.7 GHz methanol masers (Walsh et al. 1998), and water maser (Brand et al. 1994) were collected from the literature. The IRAS flux densities

were also obtained for the IRAS 18060-2005 source, using the IRAS point-source catalog (Helou & Walker 1988). The flux densities were found to be 140, 1040, 6030, and 12000 Jy at 12, 25, 60, and 100 μm , respectively.

In addition, a published map at 21 cm (Kim & Koo 2001) and integrated molecular $^{13}\text{CO}(2-1)$ line data (Beuther et al. 2011) were also utilized in the present work.

3 RESULTS

3.1 A comparison of various signposts

Figure 1 shows the W31 complex using Hi-GAL data. Different sub-regions of the complex are labeled in the figure. The location of CN 148 is denoted with a box. Figures 2, 3, and 4 provide an overview of the main characteristics of the bubble. Figure 2 illustrates the spatial distribution of dust in the region, based on the 870 μm and 24 μm continuum data. The MAGPIS 20 cm radio continuum contours (blue color; angular resolution $\sim 6''$) are drawn. We note that the 24 μm emission is saturated in the proximity of the 20 cm continuum emission. We looked at the publicly available archival WISE⁴ (Wright et al. 2010) image at 22 μm (spatial resolution $\sim 12''$) and found that it is equally saturated. The extended bipolar structure which is visible in the 21 cm data (see Introduction) appears to be traced also by the 24 μm data (Figure 2). Both the warm dust and ionized emissions are well correlated, as pointed out by Beuther et al. (2011) for the extended H II region. In general, the 24 μm emission and ionized gas are found systematically correlated in H II regions (e.g. Deharveng et al. 2010; Paladini et al. 2012). The MAGPIS 20 cm radio continuum map reveals finer features, and very weakly traces the extended emission (not seen in the figure). The outer (lower) radio contour shows an arc-like morphology whose convex surface faces the center of the bubble. The map at 20 cm traces an UCH II region (G10.30-0.15) and two additional compact H II regions, with sizes ranging from 0.22 to 0.27 pc (also highlighted in Figure 2). It is interesting to note that a small elongated ionized component (size $\sim 37''$ or 4.1 pc at a distance of 2.2 kpc) northeast of the UCH II region (separated approximately by ~ 0.15 pc) is detected in the radio map. The elongation of the feature possibly indicates that its shape was influenced by the ionized gas flow. The position of two embedded sources, 18060nr1733/s1 (O5V-O6V) and 18060nr2481/s2 (O8V-B2.5V) (Bik et al. 2005), are also marked on the figure. The association between the MIR bubble, $^{13}\text{CO}(2-1)$ molecular gas, maser positions, and the EGOs can be found in Figure 3. In this figure, both the MIR emission and the molecular gas display an almost circular morphology, except for the north and northwest directions, where the molecular density is low. The molecular gas emission is absent inside the bubble, and this empty emission region was previously reported as a molecular gas hollow by Kim & Koo (2002), which also measured its size, of the order of $2''.4$ (1.5 pc at a distance of 2.2 kpc), which is very close to the size of the MIR bubble ($\sim 2''.8$ or 1.8 pc)

¹ IRAF is distributed by the National Optical Astronomy Observatory, USA

² <http://herschel.esac.esa.int/>

³ <http://www3.mpifr-bonn.mpg.de/div/atlasgal/>

⁴ Wide Field Infrared Survey Explorer, which is a joint project of the University of California and the JPL, Caltech, funded by the NASA

estimated by Churchwell et al. (2007) using the GLIMPSE 8.0 μm emission. Becker et al. (1994) observed three radio continuum sources in the region at 6 cm and with a 4'' angular resolution. Their peak positions are marked by triangles in Figure 3. These 6 cm peaks are coincident with the peaks of the MAGPIS 20 cm radio continuum emission, including the UCH II region G10.30-0.15. The positions of an UCH II region, four 6.7 GHz methanol masers, and a water maser are coincident at the edge of the bubble, indicating their physical association. Additionally, one can notice that there are two small arc-like structures prominently seen in all IRAC images (drawn in the inset in Figure 3), facing towards the center of the bubble. The K-band cluster (including O5V-O6V and O8V-B2.5V stars) is surrounded by one of the arc-like structures, and another arc-like structure harbors a radio emission peak, situated in the northeast direction. These two arc-like features demonstrate the impact of the ionizing photons. A *JHK* color composite image (not shown here) reveals the bright clustered regions (marked in Figure 3), along with the dark extincted patches of the molecular material.

Figure 4 presents a multi-wavelength view of the bubble CN 148. The continuum data are shown at 4.5 μm , 8.0 μm , 24 μm , 70 μm , 160 μm , 250 μm , 350 μm , 500 μm , and 870 μm , from left to right in increasing order. The *Spitzer* images (4.5–24 μm) are shown only for comparison with the Hi-GAL maps. The Hi-GAL counterparts (70–500 μm) are mostly seen towards the four 6.7 GHz methanol masers (including two EGOs) at the edges of the bubble. We labeled these methanol maser emissions MME1-4 (see Figure 4). The MIPS 24 μm image is saturated towards two 6.7 GHz masers (i.e. MME2 and MME3) and MME3 is associated with an UCH II region. The 24 μm emission is seen towards the two remaining 6.7 GHz methanol masers (i.e. MME1 and MME4), which are associated with the EGOs (i.e. G10.34-0.14 and G10.29-0.13). There is no discrete 24 μm counterpart found towards the EGO G10.29-0.13, while the EGO G10.34-0.14 is blended with other 24 μm source(s) (also see Cyganowski et al. 2009). In particular, the MME4 in the southwest direction (towards EGO G10.29-0.13) appears as a compact emission rather than a diffuse source only at wavelengths longer than 70 μm (see Figure 4). This suggests the presence of a deeply embedded discrete counterpart of the EGO G10.29-0.13/MME4, at the southwest edge of the bubble. Additionally, Hi-GAL data at wavelengths longer than 70 μm trace the filament-like features in the direction northeast from the bubble. The peaks of dust continuum emission are spatially coincident along the waist of the bipolar morphology, together forming the rim of the observed bubble. The north portion of the bubble is weakly detected, possibly because the so-called *bubble* could rather be a shell with a given orientation in the sky (e.g., Beaumont & Williams 2010). Figures 2, 3, and 4 are prominently revealing only one rim of this shell.

3.1.1 Extinction maps

The visual extinction (A_V) map of the region was generated using UKIDSS NIR (JHK) photometric data, following a similar procedure to the one described by Kumar et al. (2007). The selection of the main sequence stars and the determination of the individual extinction values was per-

formed using a NIR color-color diagram (J-H/H-K) with the reddening laws of Rieke et al. (1985). The extinction map was created by Nyquist binning using the spatial distribution of the extinction values of individual stars, with a bin size of 60''. Following the suggestion of Lombardi & Alves (2001), we also performed sigma-clipping in our spatial smoothing, in order to minimize the effect of the foreground stars in the extinction map. These were identified as extremely low extinction outliers and removed from the local average. Figure 5a shows the extinction map (A_V range 3–16 mag) of the region, overlaid with the $^{13}\text{CO}(2-1)$ integrated intensity contours (Beuther et al. 2011) and the positions of the dust clumps identified from the ATLASGAL survey at 870 μm (Contreras et al. 2013). Within our selected region, we find five starless clumps from a catalog of Tackenberg et al. (2012) whose peak positions are also marked on Figure 5a. These clumps are located on the extreme outer boundary of ATLASGAL 870 μm emission, with NH_3 velocity of $\sim 13.6 \text{ km s}^{-1}$ and clump mass range of 120–420 M_\odot (see Tackenberg et al. 2012, for more detail). All dense clumps are associated with white regions in the extinction map, indicating that the visual extinction value towards these clumps should be greater than 16 mag. The average extinction value of the region is found to be ~ 7.8 mag. The extinction map traces the previously known K-band cluster with an A_V of ~ 14 mag near the IRAS position. All masers (MME1-4) appear to be located in the region having A_V greater than 16 mag. We suggest that these masers are not part of the K-band cluster, based on their spatial locations and relatively different extinction values with respect to the cluster. This interpretation is also supported by the fact that all stars in a cluster are assumed to have formed at about the same time.

3.1.2 The PAH distribution and the H II region

PAH features are known to trace photodissociation regions (or photon-dominated regions, or PDRs). PAH emission is produced in the PDR by ultraviolet (UV) photons ($6\text{eV} < h\nu < 13.6\text{eV}$) from massive stars exciting PAH molecules (Tielens et al. 2004). In our case, the presence of PAH emission allows us to infer the impact and influence of the expanding H II region on its surrounding. In recent years, ratio maps obtained using *Spitzer*-IRAC images (3.6–8.0 μm) have been utilized to trace PAH features at 3.3, 6.2, 7.7, and 8.6 μm , hence the extent of PDRs, in massive star-forming regions. In particular, the ch2 (4.5 μm) band can be used as a control band since it does not contain any known PAH line features. Therefore, IRAC ratio (ch4/ch2, ch3/ch2, and ch1/ch2) maps are generated using ch4 (8.0 μm), ch3 (5.8 μm), and ch1 (3.6 μm) bands with respect to the ch2 (4.5 μm) band. We generated ratio maps following a similar procedure as described by Povich et al. (2007) and Dewangan & Anandarao (2011). Figure 5b shows one such IRAC ratio map (ch3/ch2) overlaid with ratio contours. The bright features are indicative of PAH emission and allow us to trace the PDR surrounding the ionized gas. The ratio map also shows emission features similar to the filament-like emission seen in Hi-GAL images, in the northeast direction (see Figures 4 and 5b). The positions of the ATLASGAL dust clumps are marked in Figure 5b. The comparison between the molecular CO, cold dust, and PAH emission is shown in

Figures 5a and 5b. The molecular gas, cold dust, and PAH emission are distributed along the northeast to southwest directions (see Figures 5a and 5b). Figure 6 shows a zoomed-in continuum-subtracted $2.12 \mu\text{m}$ H_2 image using the K -band image of the bubble. The figure reveals H_2 emission at the periphery of the source. The presence of H_2 emission can be explained by either UV fluorescence or shocks. A comparison of the line intensities of the 1-0 S(1) line of H_2 at $2.12 \mu\text{m}$ to the 2-1 S(1) line of H_2 at $2.25 \mu\text{m}$ is normally used to distinguish between fluorescent and shock-excited H_2 emission. However, this source was not observed in the 2-1 S(1) line of H_2 filter. Considering the observed morphology of the H_2 features, we suggest that the origin of the H_2 emission is likely caused by UV fluorescence. There are several arc-like structures of H_2 emission, mostly facing toward the center of the bubble, indicating the exposure to strong UV radiation. Figures 2–6 suggest that the ionized region is dominant inside the bubble while the PAH, molecular gas, and cold dust emission are absent, as is expected, while the warm dust emission at $24 \mu\text{m}$ is detected in the H II region, as mentioned before. Combining the multi-wavelength characteristics of CN 148, we suggest that the existence of the curved morphology of the molecular dense material is due to the expansion of the H II region. Recently, Arce et al. (2011) predicted a circular or arc-like structure in the model for an expanding bubble (also see Churchwell 2008; Beaumont & Williams 2010), which further supports our argument on the observed molecular structure in CN 148. In summary, the molecular gas, PAH, cold dust, and H_2 emission are all coincident and constitute the evidence of star-forming material around the bubble.

3.1.3 Lyman continuum flux and ionizing feedback

In this section, we derive the spectral type of the powering star(s) associated with the extended emission as well as the three components (UCH II region, central compact peak near the IRAS position, and northeast compact peak) detected in the radio maps.

We have calculated the number of Lyman continuum photons (N_{uv}) using the radio continuum map and following the formulation of Matsakis et al. (1976):

$$N_{uv}(s^{-1}) = 7.5 \times 10^{46} \left(\frac{S_\nu}{\text{Jy}} \right) \left(\frac{D}{\text{kpc}} \right)^2 \left(\frac{T_e}{10^4 \text{K}} \right)^{-0.45} \times \left(\frac{\nu}{\text{GHz}} \right)^{0.1} \quad (1)$$

where T_e is the electron temperature, D is the distance in kpc, ν is the frequency in GHz, and S_ν is the measured total flux density in Jy. S_ν was estimated for each of the individual components using the radio continuum map at 20 cm (1.4989 GHz). Adopting $D = 2.2$ kpc and $T_e = 6800$ K (from Kim & Koo 2001), we calculated N_{uv} . Table 1 summarizes the results. The Table also lists the spectral class of each of the individual components inferred using the models of Panagia (1973, his Table 2). We find that each of the radio components is consistent with the radio spectral class of a B0V type star (see Table 1). It is worth mentioning that the spectral class of potential ionizing sources is derived by assuming that all the ionizing flux is produced by only a single star.

N_{uv} is also estimated for the extended emission using

$S_\nu = 15.92$ Jy at 21 cm (1.42 GHz) from Kim & Koo (2001), and is found to be $\sim 7.2 \times 10^{48} \text{ s}^{-1}$ ($\log N_{uv} \sim 48.86$). The MAGPIS map does not allow an accurate determination of the fluxes for extended sources ($> 60''$), due to inadequate VLA u-v coverage (see Helfand et al. 2006, for more details). Therefore, the 21 cm data was preferred over MAGPIS 20 cm radio map as it detects the extended bipolar morphology (see Figure 2). The ionizing photon flux value corresponds to a single ionizing star of spectral type O7V-O6.5V (Panagia 1973; Martins et al. 2005). It is obvious that the three B0V type stars together cannot produce sufficient ionizing radiation to explain the entire radio emission. Therefore, this extended emission is likely generated by other, more evolved sources located inside the bubble. It is to be noted that the two embedded sources 18060nr1733 (O5V-O6V) and 18060nr2481 (O8V-B2.5V) are associated with the K-band cluster located inside the bubble. The comparison of the spectral type of these two embedded sources with the radio spectral type of the powering source associated with the extended emission suggests that the spectroscopically identified O type sources can be ionizing candidates for the extended radio emission.

The radio continuum map at 20 cm is also used to estimate the electron density (n_e) of the ionized gas. The formula for “ n_e ” is given by Panagia & Walmsley (1978) under the assumption that the H II region has a roughly spherical geometry:

$$n_e(\text{cm}^{-3}) = 3.113 \times 10^2 \left(\frac{S_\nu}{\text{Jy}} \right)^{0.5} \left(\frac{T_e}{10^4 \text{K}} \right)^{0.25} \left(\frac{D}{\text{kpc}} \right)^{-0.5} \times b(\nu, T)^{-0.5} \theta_R^{-1.5} \quad (2)$$

In the equation above, S_ν , T_e , and D are defined as in Equation 1, θ_R is the angular radius in arcminutes and

$$b(\nu, T) = 1 + 0.3195 \log \left(\frac{T_e}{10^4 \text{K}} \right) - 0.2130 \log \left(\frac{\nu}{1 \text{GHz}} \right).$$

The values of S_ν and θ_R used for each of the individual components and the corresponding values of n_e are listed in Table 1. The calculation was performed for $D = 2.2$ kpc and $T_e = 6800$ K.

We have also estimated the internal pressure of a uniform density H II region (P_{HII}) to infer the ionizing feedback of massive stars on their environment. In Figures 2 and 3, we have already noticed that the ionizing sources appear to be located inside the bubble. The molecular gas and dust emissions are absent inside the bubble and are seen towards the edges of the bubble. The pressure of an H II region is estimated at $D_s = 0.9$ pc from the location of the O type stars, a distance similar to the radius of the bubble. The formula is given by $P_{HII} = \mu m_H c_s^2 \left(\sqrt{\frac{3N_{uv}}{4\pi \alpha_B D_s^3}} \right)$; where, N_{uv} is the number of ionizing photons emerging per second from the massive star, $\mu = 2.37$, c_s is the sound speed of the photo-ionized gas ($= 10 \text{ km s}^{-1}$), and α_B is the radiative recombination coefficient ($= 2.6 \times 10^{-13} \times (10^4 \text{ K}/T_e)^{0.7} \text{ cm}^3 \text{ s}^{-1}$; see Kwan 1997). One can find more details about this expression in the work of Bressert et al. (2012). Using $N_{uv} = 7.2 \times 10^{48} \text{ s}^{-1}$ and $\alpha_B = 3.4 \times 10^{-13} \text{ cm}^3 \text{ s}^{-1}$ at $T_e = 6800$ K, we calculate $P_{HII} \approx 1.9 \times 10^{-9} \text{ dynes cm}^{-2}$.

In general, typical cool molecular clouds (particle density $\sim 10^3\text{-}10^4 \text{ cm}^{-3}$ and temperature ~ 20 K) have pres-

sure values $\sim 10^{-11} - 10^{-12}$ dynes cm^{-2} (see Table 7.3 of Dyson & Williams 1980). However, the pressure exerted by the self-gravity of the surrounding molecular gas in our selected region can be different than the pressure in a cool molecular cloud. The pressure exerted by the self-gravity of the surrounding molecular gas is given by $P_{\text{cloud}} \approx \pi G \Sigma^2$, where $\Sigma (= M_{\text{cloud}}/\pi R_c^2)$ is the mean mass surface density of the cloud, M_{cloud} is the mass of the molecular gas, and R_c is the radius of the molecular region. To estimate the total dust mass of the cloud including the bubble, we utilized the ATLASGAL 870 μm map and computed its total flux over the entire cold dust emission, as seen in Figure 2. The integrated 870 μm flux is converted to the total dust mass of the cloud incorporating the gas-to-dust mass ratio (assumed to be 100), using a similar formula and inputs as mentioned in Section 3.1.4. The total dust mass of the cloud is found to be $\sim 5490 M_\odot$.

Adopting $M_{\text{cloud}} \approx 5490 M_\odot$ (assuming about 10% error in this value estimate) in a region of radius $R_c \approx 3'.0$ (or 1.9 ± 0.3 pc at a distance of 2.2 ± 0.3 kpc), we find a surface density $\Sigma \approx 0.10 \pm 0.03 \text{ g cm}^{-2}$ and $P_{\text{cloud}} \approx 2.1 \pm 1.4 \times 10^{-9}$ dynes cm^{-2} , which is comparable to the value for P_{HII} that we obtained earlier.

We can also estimate the pressure contributions from the radiation pressure ($P_{\text{rad}} = L_{\text{bol}}/4\pi c D_s^2$) and the stellar wind ram pressure ($P_{\text{wind}} = \dot{M}_w V_w/4\pi D_s^2$). However, we do not have any specific information about the mass-loss rate (\dot{M}_w) and the wind velocity (V_w) of the powering star(s), and the bolometric luminosity (L_{bol}) of the region. The total FIR luminosity of IRAS 18060-2005 derived using the IRAS fluxes (see Casoli et al. 1986) is $\sim 0.94 \times 10^5 L_\odot$ at a distance of 2.2 kpc. In order to derive P_{wind} and P_{rad} in the region, we have substituted the values $\dot{M}_w = 3.74 \times 10^{-7} M_\odot \text{ yr}^{-1}$ (for O6.5V star; Vink et al. 2001), $V_w = 2200 \text{ km s}^{-1}$ (for O6.5V star; Kudritzki et al. 2000), and $L_{\text{bol}} \approx 10^5 L_\odot$ (see Beuther et al. 2011; Lumsden et al. 2013), in the above equations. We find $P_{\text{wind}} \approx 5.4 \times 10^{-11}$ dynes cm^{-2} and $P_{\text{rad}} \approx 1.3 \times 10^{-10}$ dynes cm^{-2} at $D_s = 0.9$ pc from the location of the O type sources. This calculation reveals that, in this case, the pressure of the H II region dominates over the radiation pressure and the stellar wind pressure, even assuming a factor of 10 uncertainty associated with the estimated values. Summing up all the pressure components (i.e. P_{HII} , P_{rad} , and P_{wind}), we find that the total pressure, P_{total} , is $\approx 2.1 \times 10^{-9}$ dynes cm^{-2} . Therefore, the total pressure is in equilibrium with the pressure exerted by the surrounding, self-gravitating molecular cloud ($\approx 10^{-9}$ dynes cm^{-2}), and suggests that the surrounding molecular cloud has been compressed to increase the pressure and balance the total pressure (P_{total}). This, in turn, could trigger the initial collapse and fragmentation of a large molecular cloud. Such a scenario is supported by the presence of several dense clumps surrounding the H II region. Altogether, the pressure of the H II region could be responsible for the expansion of the bubble and have significant influence on the surrounding environment.

3.1.4 Dust clumps

In Section 3.1.1 we showed the spatial distribution of dust emission in CN 148 using the ATLASGAL 870 μm data. Contreras et al. (2013) describe the creation of the ATLAS-

GAL compact source catalog, based on the source extraction algorithm SExtractor and using a detection threshold of 6-sigma. Noteworthy, the ATLASGAL catalog does not provide masses for the individual sources. In this Section, we provide an estimate of the mass of the ATLASGAL sources in our selected region. Within our selected region, we find 14 sources from the ATLASGAL catalog. For a distance of 2.2 kpc, all the compact sources are clumps smaller than 1 pc (see Table 2). For a reliable mass estimate, the observational knowledge about the temperatures within the clumps is crucial. Wienen et al. (2012) derived kinetic and rotational temperatures from NH_3 observations of the ATLASGAL sources. For our selected region, this information is available for only six clumps. The clump mass was estimated using the following formula (Hildebrand 1983):

$$M = \frac{D^2 S_\nu R_t}{B_\nu(T_D) \kappa_\nu} \quad (3)$$

where S_ν is the integrated 870 μm flux (Jy), D is the distance (kpc), R_t is the gas-to-dust mass ratio (assumed to be 100), B_ν is the Planck function for a dust temperature T_D , and κ_ν is the dust absorption coefficient. The clump masses and their associated errors are listed in Table 2, assuming $\kappa_\nu = 1.85 \text{ cm}^2 \text{ g}^{-1}$ (Schuller et al. 2009), $D = 2.2 \pm 0.3$ kpc and $T_D = 20$ K (average rotational temperature of six ATLASGAL clumps; see Table 2). Table 2 also includes the integrated 870 μm fluxes (with uncertainties), clump effective radius, and $\text{NH}_3(3,3)$ velocities, linewidths, rotational temperature and kinetic temperature. The total mass of 14 clumps is found to be $\sim 7264 M_\odot$ and clump masses vary between 110 and $1533 M_\odot$. Interestingly, four ATLASGAL clumps are physically associated with the 6.7 GHz methanol maser, and two of them are also physically associated with the EGOs. These clumps show high kinetic temperature as derived from the NH_3 line parameters (see Table 2).

In a previous study of the W31 region, Beuther et al. (2011) found several 870 μm cold dust emission clumps in the ATLASGAL survey, and estimated their masses using an average dust temperature of 50 K and a distance of 6 kpc. These authors used the CLUMPFIND algorithm at 3-sigma contour levels (210 mJy/beam) to extract the clumps from 870 μm map. They also adopted the dust absorption coefficient $\kappa_{870} \approx 0.8 \text{ cm}^2 \text{ g}^{-1}$ and a gas-to-dust mass ratio of 186, in their calculation. Within our selected region, Beuther et al. (2011) identified 20 dust clumps with the total mass of $\sim 46440 M_\odot$ with a mass range between 168 and $8187 M_\odot$, at a distance of 6 kpc. One can notice the difference in number of clumps identified between the work of Beuther et al. (2011) and Contreras et al. (2013), probably due to the selection of different clump extraction algorithms and different threshold values. A large difference in clump masses is also caused by the different choice of distance, dust temperature, dust absorption coefficient and gas-to-dust mass ratio in the calculation.

The calculation of dust clump masses in this work therefore benefits from a better knowledge of the distance to the source and the availability of the NH_3 line parameters.

3.2 The YSO content of CN 148

In the following, we present the identification and selection of young stellar populations using UKIDSS and GLIMPSE

Table 1. Physical parameters of the ionized components associated with the H II region, G10.3-0.1, using a 20 cm high resolution continuum map (see Figure 3).

Source	RA [2000]	Dec [2000]	Angular radius (θ_R in arcminutes)	Total flux (S_ν in Jy)	$\log N_{uv}$ (s^{-1})	Spectral Type	Electron density (n_e in cm^{-3})
UCH II region	18:08:55.9	-20:05:54	0.36	1.008	47.66	B0V–O9.5V	936.93
Central compact peak	18:09:00.4	-20:05:10	0.42	1.382	47.80	B0V–O9.5V	862.83
Northeast compact peak	18:09:01.6	-20:04:38	0.34	0.724	47.52	B0.5V–B0V	850.42

Table 2. Dust clumps from the ATLASGAL survey at 870 μm (Contreras et al. 2013) in our selected region (also see Figure 5). Clump masses were estimated using integrated fluxes for a dust temperature = 20 K at a distance of 2.2 ± 0.3 kpc. NH_3 parameters (velocity ($v(3,3)$), linewidth ($dv(3,3)$), rotational temperature (Trot) and kinetic temperature (Tkin)) of 6 ATLASGAL clumps were taken from the literature for our selected region (see Wienen et al. 2012). Superscript asterisk symbol (*) denotes the clumps associated with 6.7 GHz methanol masers. Association of the EGOs with the dust clumps are highlighted by superscript “†” (see the text).

ID	RA [2000]	Dec [2000]	ATLASGAL designation	Effective Radius [pc]	Integrated 870 μm Flux [Jy]	Clump Mass [M_\odot]	$v(3,3)$ [km/s]	$dv(3,3)$ [km/s]	Trot [K]	Tkin [K]
c1	18:08:41.5	-20:07:34	010.249-00.111	0.83	20.37 ± 3.34	543.8 ± 185.9	14.47	5.71	16.54	19.18
c2	18:08:31.7	-20:05:37	010.259-00.062	0.19	4.14 ± 0.88	110.5 ± 40.6	—	—	—	—
c3	18:08:47.3	-20:06:20	010.278-00.121	0.69	16.64 ± 2.78	444.2 ± 152.5	—	—	—	—
c4	18:08:46.6	-20:05:49	010.284-00.114	0.35	22.39 ± 3.64	597.7 ± 203.9	—	—	—	—
c5	18:08:57.8	-20:07:10	010.286-00.164	0.44	9.95 ± 1.76	265.6 ± 92.5	11.84	4.84	14.63	16.42
c6*†	18:08:49.2	-20:05:54	010.288-00.124	0.16	10.74 ± 1.88	286.7 ± 99.6	—	—	—	—
c7*	18:08:55.7	-20:06:00	010.299-00.147	0.73	54.18 ± 8.41	1446.3 ± 488.5	12.69	6.75	22.98	30.20
c8	18:09:17.3	-20:07:17	010.321-00.231	0.35	5.21 ± 1.04	139.1 ± 50.1	—	—	—	—
c9*	18:09:01.7	-20:05:08	010.323-00.161	0.91	57.42 ± 8.90	1532.8 ± 517.6	12.41	3.45	24.05	32.36
c10	18:09:05.0	-20:05:08	010.329-00.172	0.33	10.83 ± 1.90	289.1 ± 100.5	—	—	—	—
c11*†	18:09:00.0	-20:03:35	010.342-00.142	0.35	17.58 ± 2.91	469.3 ± 160.8	12.34	4.07	22.99	30.23
c12	18:09:06.9	-20:04:21	010.344-00.172	0.37	12.89 ± 2.21	344.1 ± 118.9	—	—	—	—
c13	18:09:03.1	-20:03:04	010.356-00.149	0.51	24.32 ± 3.93	649.2 ± 221.2	11.23	2.61	17.50	20.64
c14	18:09:17.8	-20:02:44	010.388-00.196	0.16	5.47 ± 1.08	146.0 ± 52.4	—	—	—	—

data, to learn about the star formation process around the bubble CN 148.

3.2.1 Identification of YSOs

The identification of YSOs is based on their IR excess emission, observed due to the presence of natal envelopes or circumstellar disks. The IR identification of these YSOs can be affected by various possible contaminants (e.g. broad-line active galactic nuclei (AGNs), PAH-emitting galaxies, shocked emission blobs/knots, and PAH-emission-contaminated apertures). Gutermuth et al. (2009) have proposed detailed criteria, using the four IRAC bands, to identify YSOs and remove the contaminants. It has been observationally reported that the interstellar extinction curve is relatively flat between 4.5 and 5.8 μm bands (Indebetouw et al. 2005; Flaherty et al. 2007). Therefore, the [4.5]–[5.8] color space is much less influenced by dust extinction and this color has been used for YSO classification by Gutermuth et al. (2009). In order to identify YSOs and likely contaminants, we applied the various color conditions suggested by Gutermuth et al. (2009). The identified YSOs were further classified into different evolutionary stages (i.e. Class I, Class II, and Class III), using the slopes of the IRAC spectral energy distribution (SED) (α_{IRAC}) measured from 3.6 to 8.0 μm (e.g., Lada et al. 2006). The α_{IRAC} conditions (see Billot et al. 2010, for more details) were considered for Class I YSOs ($\alpha_{IRAC} > -0.3$), for Class II

YSOs ($-0.3 > \alpha_{IRAC} > -1.6$), and for Class III sources ($-1.6 > \alpha_{IRAC} > -2.56$). The IRAC color-color diagram ([3.6]–[4.5] vs [5.8]–[8.0]) is shown in Figure 7a for all the identified sources. Using this approach, we obtain 50 YSOs (23 Class 0/I; 27 Class II), 630 photospheres, and 79 contaminants in the selected region around the bubble CN 148.

Compared to the two shorter wavelengths (3.6 and 4.5 μm), the 5.8 and 8.0 μm IRAC bands are more sensitive to diffuse emission than point sources. Therefore, IRAC 3.6 and 4.5 μm bands were combined with UKIDSS NIR HK photometry (i.e. WFCAM-IRAC) to identify additional YSOs, mainly when sources were not detected in the IRAC 5.8 and/or 8.0 μm bands. We adopted the method developed by Gutermuth et al. (2009) to identify YSOs using WFCAM-IRAC (H, K, 3.6, and 4.5 μm) data (see Gutermuth et al. 2009, for more details). In this scheme, the dereddened colors ($[K - [3.6]]_0$ and $[3.6 - [4.5]]_0$) were calculated using the color excess ratios listed in Flaherty et al. (2007). The classified Class I and Class II YSOs were further checked for possible dim contaminants by means of the dereddened 3.6 μm magnitudes (i.e. $[3.6]_0 < 14.5$ for Class II and $[3.6]_0 < 15$ for Class I), which were estimated using our extinction measurements and the reddening law from Flaherty et al. (2007). Following this method, we found 191 additional YSOs (27 Class I and 164 Class II; see Figure 7b).

We also made use of an IRAC color-color diagram ([3.6]–[4.5] vs. [4.5]–[5.8]) to identify protostars when sources were either not detected or saturated in the 8.0 μm band. The

protostars were selected using the criteria $[3.6]-[4.5] \geq 0.7$ and $[4.5]-[5.8] \geq 0.7$ from Hartmann et al. (2005) and Getman et al. (2007). With this procedure, we identified 16 protostars (see Figure 7c).

There are a large number of sources detected only in the NIR regime, which are not present in the GLIMPSE data. Therefore, we have selected very red sources having $H-K > 2.2$ using the color-magnitude ($K/H-K$) diagram (see Figure 7d), and found 114 sources. This cut-off criterion allows us to identify very deeply embedded sources.

Combining the identification from all the four methods described above, a total of 371 YSOs are obtained in the region. The positions of all YSOs are plotted in Figure 8a.

The above methods can lead to contamination from other intrinsically “red sources” such as asymptotic giant branch (AGB) stars (Whitney et al. 2008; Robitaille et al. 2008). We checked the possibility of intrinsically “red sources” as well as AGB contaminations in our YSO sample, following the criteria suggested by Robitaille et al. (2008), using $4.5 \mu\text{m}$, $8.0 \mu\text{m}$, and $24 \mu\text{m}$ photometry data. Only 50 out of the 371 YSOs have detections in the $4.5 \mu\text{m}$ and $8.0 \mu\text{m}$ bands. We find 21 out of these 50 YSOs ($\sim 42\%$) to be possible intrinsically “red sources”. These “red sources” were further checked for any likely AGB contaminations, based on their detections in the MIPS GAL $24 \mu\text{m}$ image. We find no AGB contamination among the selected “red sources”. Additionally, AGB stars can also be disentangled from YSOs by applying a color-color criterion based on the Hi-GAL $70\text{--}350 \mu\text{m}$ flux densities (e.g., Veneziani et al. 2013). In our case, the application of the Veneziani et al. (2013)’s AGB identification method retrieved no AGB candidate.

3.2.2 Spatial distribution of the YSOs and their clustering

In order to study the spatial distribution of the YSOs, we have constructed the YSO surface density map, following the method suggested by Gutermuth et al. (2009). The surface number density at the i^{th} grid point is defined as $\rho_i = (n - 1)/A_i$ with fractional uncertainty of $(n - 2)^{-0.5}$ (Casertano & Hut 1985), where A_i is the surface area defined by the radial distance to the n nearest-neighbour. We computed the 6^{th} nearest-neighbour (NN) density map projected on a $5''$ grid at a distance of 2.2 kpc. It is shown as contours on Figure 8. The choice of $n = 6$ was found to be a good compromise between the resolution and sensitivity of the surface density calculation (e.g. Casertano & Hut 1985; Gutermuth et al. 2009). The contour levels are drawn at 10 YSOs/ pc^2 (2.2σ), 15 YSOs/ pc^2 (3.2σ), 20 YSOs/ pc^2 (4.3σ), 30 YSOs/ pc^2 (6.5σ), and 40 YSOs/ pc^2 (8.6σ), increasing from the outer to the inner region. In Figure 8a, the overlay demonstrates the correlation of molecular gas emission with that of YSO surface density. The spatial distribution of the YSOs, superimposed on the visual extinction map, is shown in Figure 8b.

To study the YSO clustering, we need to separate the clustered and scattered YSO populations. This analysis can be done by determining the empirical cumulative distribution (ECD) of YSOs as a function of NN distance. The ECD allows us to choose a cutoff length (also referred to as the distance of inflection d_c) that separates the low-density com-

ponents (see Chavarría et al. 2008; Gutermuth et al. 2009, for more details). Using the ECD analysis, we find $d_c \sim 0''.0122$ (or 0.47 pc at a distance of 2.2 kpc) to trace the cluster members within the contour level of 10 YSOs/ pc^2 in the entire region. More details on the cluster identification can be found in the work of Bressert et al. (2010). Considering the surface density level of 10 YSOs/ pc^2 , about 41% of the YSOs (i.e. 154 from a total of 371 YSOs) are found in the clusters. We identified 13 clusters and label them in Figure 9a. This finding reveals the embedded clusters of YSOs (having extinction greater than ~ 16 mag), mostly concentrated in the northeast to southwest, following the molecular gas emission around the bubble (see Figures 8 and 9a). The spatial locations of the clusters clearly demonstrate that star formation is concentrated in the high extinction regions around CN 148.

All the clusters are listed in Table 3, along with the number of members for each cluster. We notice age spread in the clusters with respect to the bubble, based on the relative distribution of Class I and Class II YSOs in each cluster. In order to trace an apparent age gradient in the clusters, we constructed the surface density maps of Class I and Class II YSOs (including sources having $H-K > 2.2$) separately, following the procedure described above. The surface density maps of Class I and Class II YSOs are shown in Figure 9b. The surface density of Class I YSOs is found to vary between 0.16 and 17.11 YSOs/ pc^2 with a dispersion (σ) of 1.41 and it is drawn at contour levels of 3.5, 6, 8, and 10 YSOs/ pc^2 . The surface density of Class II YSOs varies between 0.67 and 40.68 YSOs/ pc^2 , with a standard deviation of 3.37 and is drawn at contour levels of 10 and 15 YSOs/ pc^2 .

Considering the observational evolutionary classification of YSOs, one can suggest that the clusters associated with Class I YSOs are relatively younger than those associated with Class II YSOs. The Class I cluster, “g13”, including an EGO (G10.34-0.14), is located at the northeast edge of the bubble. The Class II clusters, “g7, g8, and g9”, are spatially distributed in the northeast direction, further away from the Class I cluster “g13”. Therefore, in the northeast direction, there appears to be an apparent age gradient in the clusters with respect to the bubble. The “g2 and g11” clusters contain both Class I and Class II YSOs (see Figures 9a and 9b). The cluster “g11” contains an UCH II G10.30-0.15 region, whereas the cluster “g2” is associated with an EGO (G10.29-0.13) at the southwest edge of the bubble. Cyganowski et al. (2011), based on VLA observations, found no 3.6 cm and 1.3 cm emission towards this EGO (G10.29-0.13). It is worth noting that both the UCH II and the EGO (G10.29-0.13) are associated with a 6.7 GHz methanol maser. Chambers et al. (2009) pointed out that the EGO represents the earliest phase of MSF before the onset of a hyper-compact(HC)/UCH II phase. In the later phase of evolution, an EGO phase ends with the formation of the HC/UCH II region. Due to these observational facts, we can suggest that the cluster “g11” is relatively more evolved, compared to the cluster “g2”. The Class II clusters “g3 and g4” are located at the southwest of cluster “g2”, suggesting an apparent age gradient in the clusters situated in the southwest direction with respect to the bubble.

Overall, these observational characteristics indicate that the clusters at the edges of the bubble (both north-

Table 3. The list of identified embedded clusters and their respective YSO populations. The YSO populations (Class I and Class II) are identified using four methods (i.e., four IRAC bands, three IRAC bands, WFCAM-IRAC (H, K, 3.6 μ m and 4.5 μ m) and H-K > 2.2). All the clusters are labeled in Figure 9a (see the text for more details).

Cluster ID	Class I			Class II		Total		Red sources H-K > 2.2
	Four IRAC	WFCAM-IRAC	Three IRAC	Four IRAC	WFCAM-IRAC	Class I	Class II	
g1	0	0	0	0	4	0	4	0
g2	2	0	0	3	4	2	7	4
g3	1	1	1	1	7	3	8	2
g4	1	0	0	1	1	1	2	3
g5	0	0	0	0	2	0	2	2
g6	0	0	0	0	2	0	2	4
g7	0	0	0	0	4	0	4	7
g8	0	0	0	0	3	0	3	1
g9	1	1	0	0	3	2	3	3
g10	0	1	0	0	4	1	4	2
g11	0	2	1	0	2	3	2	5
g12	0	1	0	0	4	1	4	6
g13	5	3	2	3	2	10	5	1

east and southwest) are relatively younger than the clusters located further away from the bubble.

3.2.3 Masers and the evolutionary stages of MSF

It was pointed out in the Introduction that the masers (four methanol and one water), an UCH II region, and two EGOs are physically associated with the bubble CN 148. It was also noted earlier that all the 6.7 GHz masers are associated with high-mass 870 μ m dust continuum clumps (see Table 2). It is interesting to recall that the masers MME1, MME3, and MME4 are associated with the EGO G10.34-0.14, EGO G10.29-0.13, and the UCH II region, respectively. Our photometric analysis reveals a Class I YSO towards the maser MME2. The position of this Class I YSO coincides with the maser position to within 2''. Moisés et al. (2011) also identified an embedded source towards this maser and suggested that the source is a probable MYSO candidate. It is found to be saturated in the 8 and 24 μ m images and is coincident with the ATLASGAL clump “c9” (see Figure 5). The outcome of the SED modelling of the IR-counterpart (IRc) of MME2 also supports the argument that this source is a MYSO (see Section 3.2.4). Based on the results, we can suggest the presence of different early evolutionary stages of MSF (MYSO, EGOs, and a relatively evolved UCH II region) at the edges of the bubble. These stages do not appear to be associated with the K-band IR cluster located inside the bubble.

3.2.4 The SED modelling

We modelled the SED of the IRc of MME2 ($\alpha_{2000} = 18^h09^m01.2^s$, $\delta_{2000} = -20^\circ05'09''$) using an on-line SED modeling tool (Robitaille et al. 2006, 2007). The model grid consists of 20,000 SED models from Robitaille et al. (2006) computed using two-dimensional radiative transfer Monte Carlo simulations. Each YSO model provides the output SEDs for 10 inclination angles, covering a range of stellar masses from 0.1 to 50 M_\odot . These models assume an accretion scenario with a central source associated with rotationally flattened infalling envelope, bipolar cavities, and a flared accretion disk, all under radiative equilibrium. We only select those models which satisfy the criterion: $\chi^2 - \chi_{best}^2 < 5$, where χ^2 is taken per data point. The SED fitted models

for the IRc of MME2 are shown in Figure 10. The IRc is detected at wavelengths longer than 1.25 μ m. The weighted mean values of the luminosity and mass are $2355 \pm 940 L_\odot$ and $7.7 \pm 2.4 M_\odot$, respectively. Our SED result suggests that the IRc of MME2 could be a MYSO.

4 DISCUSSION

Our present study expands upon the results of Beuther et al. (2011) and Kim & Koo (2001, 2002) with a better distance estimate to CN 148 and a detailed analysis of its stellar content. The ATLASGAL cold dust clumps (c1–c14) and previously published CO data (Beuther et al. 2011) show the fragmentation of dense material in the region (see Figure 5). Six of these cold dust clumps, detected in NH₃ emission, are located at the edge of the bubble (see Table 2), representing a high density (critical density $\sim 10^4 \text{ cm}^{-3}$) component of the molecular cloud. These clumps are found to be massive with a total dust mass of $\sim 4907 M_\odot$. The clumps associated with 6.7 GHz masers show higher rotational and kinetic temperatures, and also display large line widths of the NH₃(3,3) line, which are indirectly suggestive of increased star formation activity (also see, Wienen et al. 2012). In addition, five starless clumps are also spatially located on the extreme outer boundary of ATLASGAL 870 μ m emission, away from the inner edges of the bubble (see Figures 5a and 9). We also note that there is an absence of IR excess source(s) in these starless clumps. All these dust clumps, including the starless ones, were exclusively found in regions with $A_V > 16 \text{ mag}$.

In this paper, we have investigated the population of young stars using NIR and MIR data, which was lacking from previous studies of this region. Based on the identification of YSOs, we studied their spatial distribution to explore the details of the star formation process in CN 148. The surface density of YSOs is well correlated with the star-forming material in the PDR, mostly concentrated in the northeast to southwest axis with respect to the bubble (see Figures 8 and 9). We have observed that the clusters at the edges of bubble (in northeast and southwest directions) are relatively younger than the clusters located further away from the bubble (see Figure 9b).

As mentioned earlier, the early evolutionary stages of

MSF (MYSO, EGOs, and relatively evolved UCH II region) can be seen at the edges of the bubble associated with the 6.7 GHz methanol masers. Beuther et al. (2011) also pointed out three different evolutionary stages of star formation such as a more evolved IR cluster, high-mass protostellar objects, and high-mass starless clump candidates, and suggested their formation due to the triggering process. This study reveals that the bubble CN 148 is one of the rare single targets, which contains different early phases of MSF at the edges, including starless clumps as well as significant clustering of YSOs.

Recently, Kendrew et al. (2012), Thompson et al. (2012), and Deharveng et al. (2010) studied a large number of MIR bubbles to understand the statistical importance of triggered star formation and suggested the formation of 14–30% of massive stars in the Milky Way by the triggering process. Including these recent statistics, it is immediately evident that some fraction of these MIR bubbles associated with H II regions can be sites of triggered star formation.

Altogether, the existence of an apparent age gradient in YSO clusters, their spatial distribution in the PDR, and different early evolutionary stages of MSF around the bubble powered by the O type stars, suggest their origin to be influenced by an H II region expanding into the surrounding ISM. All these observational evidences support the notion that the star formation triggered by feedback such as from H II regions may be an important mechanism for high-mass star formation (e.g., Deharveng et al. 2010) in this particular region.

5 SUMMARY AND CONCLUSIONS

We studied the star formation process around the bubble CN 148, associated with the H II region G10.3-0.1, using multi-wavelength observations. This work provides a careful look at various archival public data surveys (e.g. MAGPIS, ATLASGAL, Hi-GAL, MIPSGAL, GLIMPSE, UWISH2, 2MASS, and UKIDSS), along with previously published radio 21 cm continuum and molecular line (CO) observations of the source. This study used a more appropriate distance to CN 148. The important conclusions of this work are as follows:

(i) The arc-shaped distribution of molecular CO gas along with cold dust emission and PAH features trace a PDR around the H II region.

(ii) The presence of a PDR and several arc-like structures of H₂ emission, directly suggests the impact and influence of the H II region on its surrounding. The observed curvature morphology of the molecular dense material is likely caused by the expansion of the H II region.

(iii) High-resolution MAGPIS 20 cm radio continuum data trace three distinct compact components including an UCH II region G10.30-0.15, and each of them is found to be powered by early B type stars.

(iv) Hi-GAL images (70–500 μ m) show a very similar morphology to the one seen in the ATLASGAL 870 μ m map. Filament-like features are seen in the Hi-GAL images,

in the direction northeast from the bubble. Using the ATLASGAL survey at 870 μ m, 14 cold dust clumps were found with a total dust mass of $\sim 7264 M_{\odot}$ and all of them are associated with A_V larger than ~ 16 mag. The detection of several high-mass as well as dense 870 μ m cold dust continuum clumps, along with the CO emission, show fragmentation of the dense molecular material along the bubble.

(v) Five starless clumps are also spatially located at the extreme outer boundary of ATLASGAL 870 μ m emission, away from the edges of the bubble.

(vi) Four 6.7 GHz methanol masers (MME1-4) were detected at the edges of the bubble, two of which (MME1 and MME4) are physically associated with the EGOs in the northeast (G10.34-0.14) and southwest (G10.29-0.13) directions. Previously, these EGOs were characterized as MYSOs, associated with outflow activity and lack of radio continuum emission. The two remaining 6.7 GHz methanol masers (MME2 and MME3) are physically linked with a massive protostar candidate (mass $\sim 7.7 \pm 2.4 M_{\odot}$) and the UCH II region G10.30-0.15. These characteristics favour the presence of different early stages of MSF at the edges of the bubble.

(vii) *Spitzer*-IRAC and NIR photometric data revealed 371 YSOs in the region. 41% (i.e. 154 from a total of 371 YSOs) of these YSOs are present in 13 clusters, with A_V larger than ~ 16 mag, and are spatially distributed in the northeast to southwest directions. The density distribution of all YSOs is well correlated with that of the molecular gas and cold dust emission in the PDR.

(viii) The surface density of Class I and Class II YSOs reveals that the clusters at the edges of the bubble (both northeast and southwest) are relatively younger than the clusters located further away from the bubble.

(ix) The distribution of molecular gas, cold dust emission, 6.7 GHz masers, EGOs, starless clumps, and an apparent age spread in YSO clusters provide an argument for the existence of star formation activity around the bubble, which is triggered by the expanding H II region.

Based on all the observational evidences presented in this paper, we suggest that the bubble CN 148 is a site of possible triggered star formation, resulting from the expansion of the H II region.

ACKNOWLEDGMENTS

We thank the anonymous referee for a critical reading of the manuscript and several useful comments and suggestions, both for the present manuscript and from earlier submissions to MNRAS journal, which greatly improved the scientific contents of the paper. This work is based on data obtained as part of the UKIRT Infrared Deep Sky Survey and UWISH2 survey. This publication made use of data products from the Two Micron All Sky Survey (a joint project of the University of Massachusetts and the Infrared Processing and Analysis Center / California Institute of Technology,

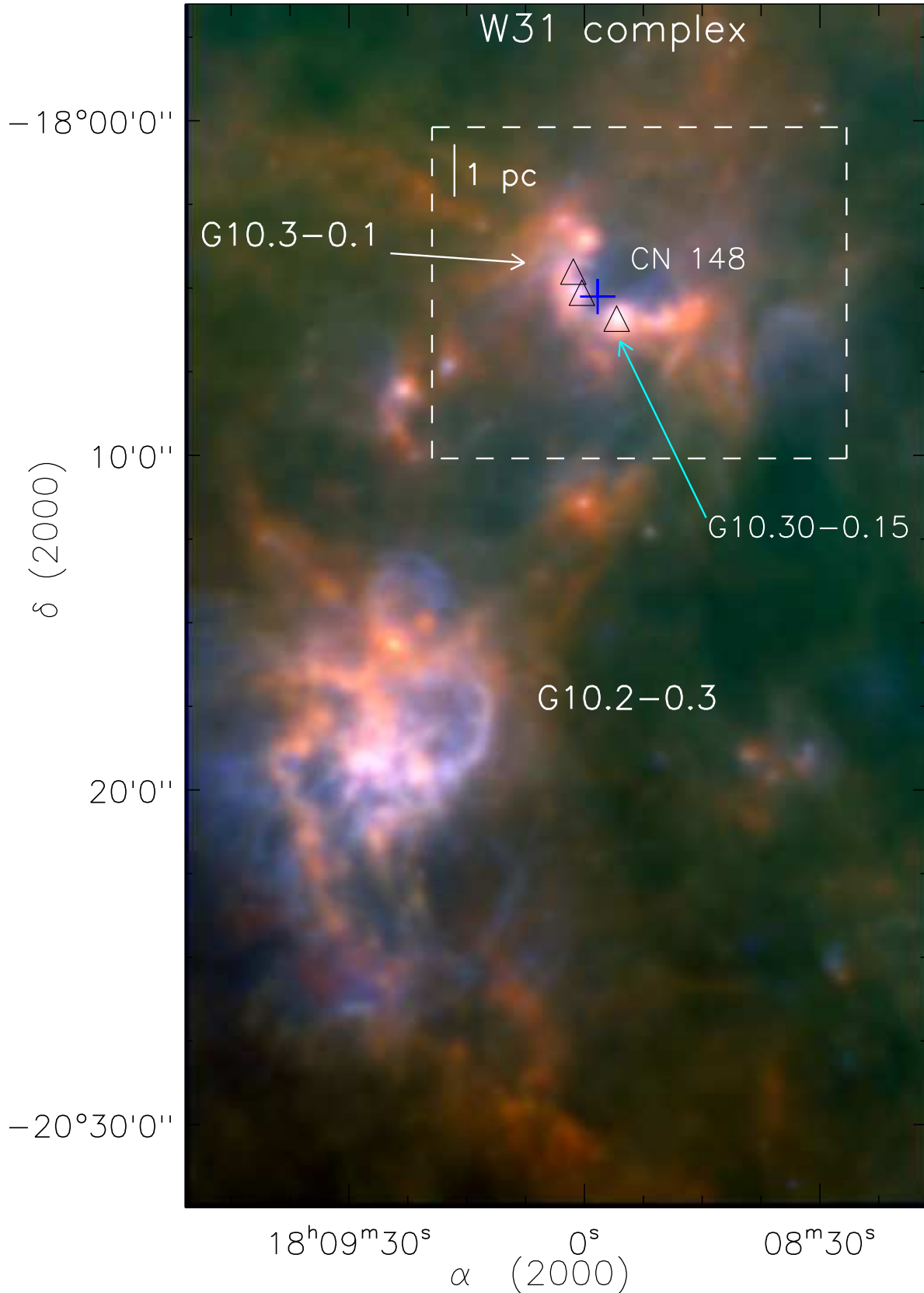


Figure 1. *Herschel* Hi-GAL continuum images (350 μm (red), 160 μm (green), and 70 μm (blue)) in log scale of the W31 region. The sub-regions G10.2-0.3 and G10.3-0.1 of the W31 complex are labeled in the figure. The region selected in this paper is highlighted by the white dashed box in figure. The positions of IRAS 18060-2005 (+) and three 6 cm radio detections (Δ) are also marked in the selected region. The scale bar on the top left in the G10.3-0.1 region shows a size of 1 pc at a distance of 2.2 kpc.

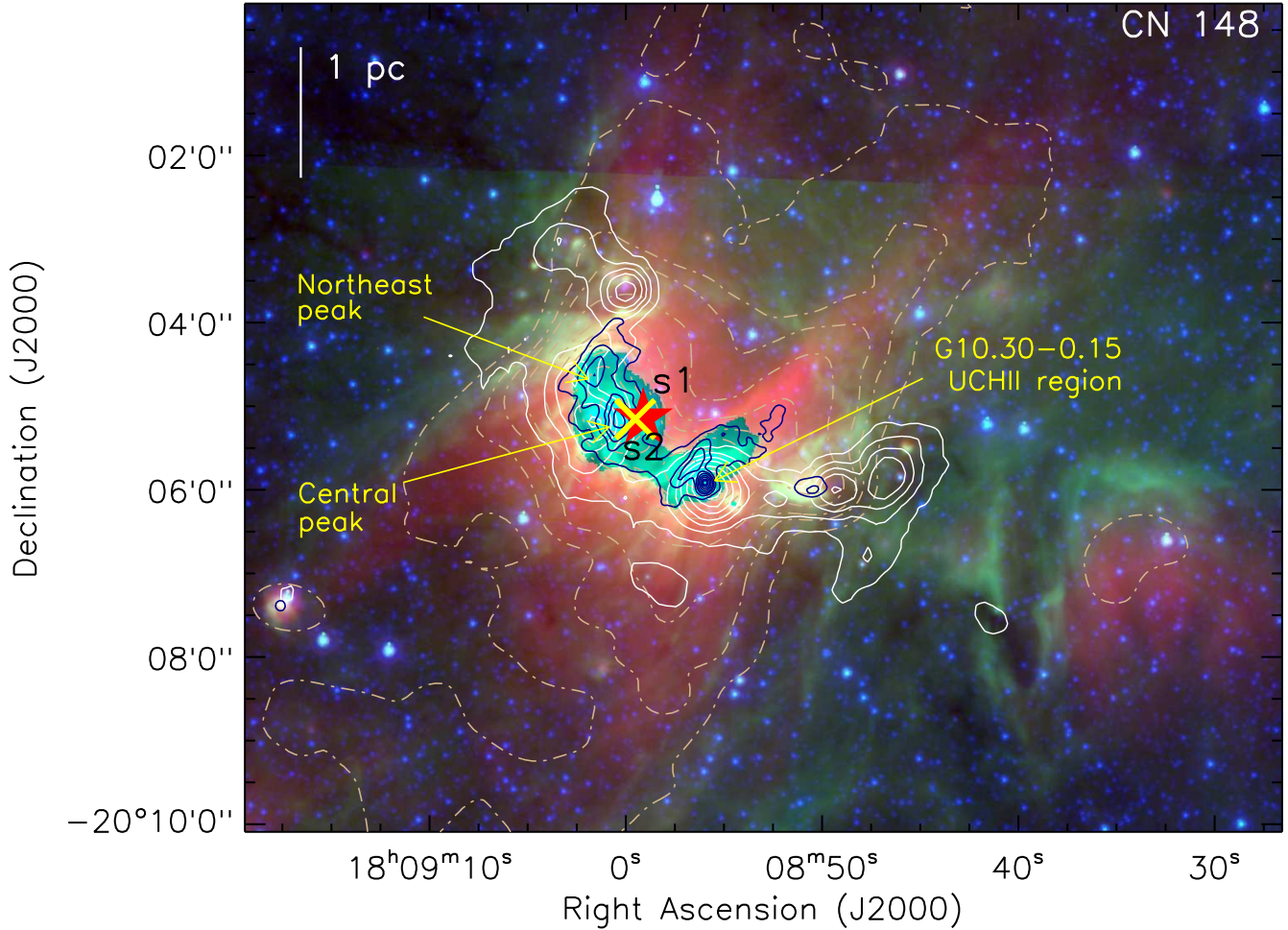


Figure 2. Three color composite image of the bubble CN 148 in the G10.3-0.1 region (size of the selected field $\sim 12'.4 \times 9'.9$; central coordinates: $\alpha_{2000} = 18^h 08^m 53^s.0$, $\delta_{2000} = -22^\circ 05' 08''.6$) from *Spitzer* observations with MIPS GAL 24 μm (red), GLIMPSE 8 μm (green), and 4.5 μm (blue). ATLASGAL 870 μm emissions are overlaid by white contours with the levels of 0.76, 1.51, 2.27, 3.03, 4.17, 5.30, 6.44, and 7.19 Jy/beam. New MAGPIS 20 cm radio continuum (angular resolution $\sim 6''$) contours in navy blue color are also overlaid with 10, 20, 30, 40, 55, 70, 85, and 95% of the peak value i.e. 0.206 Jy/beam. Tan color dot-dash contours delineate the previously published 21 cm radio continuum emission (spatial resolution $\sim 37'' \times 25''$; from Kim & Koo 2001) with 1, 3, 5, 10, 20, 30, 40, 55, 70, 85, and 95% of the peak value i.e. 1.425 Jy/beam. The locations of an UCH II region G10.30-0.15 and two compact components are also shown in the figure (see Table 1). Two candidates, s1 (18060nr1733) and s2 (18060nr2481), identified as O-stars (see the text) are also marked by big filled “ \star (red)” and “ \times (yellow)” symbols in the figure, respectively. The scale bar on the top left shows a size of 1 pc at a distance of 2.2 kpc.

funded by NASA and NSF), archival data obtained with the *Spitzer* Space Telescope (operated by the Jet Propulsion Laboratory, California Institute of Technology under a contract with NASA). The ATLASGAL project is a collaboration between the Max-Planck-Gesellschaft, the European Southern Observatory (ESO) and the Universidad de Chile. LKD is supported by the grant SFRH/BPD/79741/2011, from FCT (Portugal). We thank Dirk Froebrich for providing the narrow-band H_2 image through UWISH2 survey. We also thank Henrik Beuther for providing the integrated molecular $^{13}\text{CO}(2-1)$ fits file.

REFERENCES

- Arce H. G., Borkin M. A., Goodman A. A., Pineda J. E., Beaumont C. N., 2011, *ApJ*, 742, 105
- Beaumont C. N., Williams J. P., 2010, *ApJ*, 709, 791
- Becker R. H., White R. L., Helfand D. J., Zoonematkermani S., 1994, *ApJS*, 91, 347
- Benjamin R. A., Churchwell E., Babler B. L., et al., 2003, *PASP*, 115, 953
- Beuther H., et al., 2011, *A&A*, 531, 26
- Bik A., Kaper L., Hanson M. M., Smits M., 2005, *A&A*, 440, 121
- Billot N., Noriega-Crespo A., Carey S., Guieu S., Shenoy S., Paladini R., Latter W., 2010, *ApJ*, 712, 797
- Brand J., et al., 1994, *A&AS*, 103, 541
- Bressert E., Bastian N., Gutermuth R., Megeath S. T., Allen L., et al., 2010, *MNRAS*, 409, 54
- Bressert E., Ginsburg A., Bally J., Battersby C., Longmore S., Testi L., 2012, *ApJ*, 758, 28
- Carey S. J., et al., 2005, *BAAS*, 37, 1252

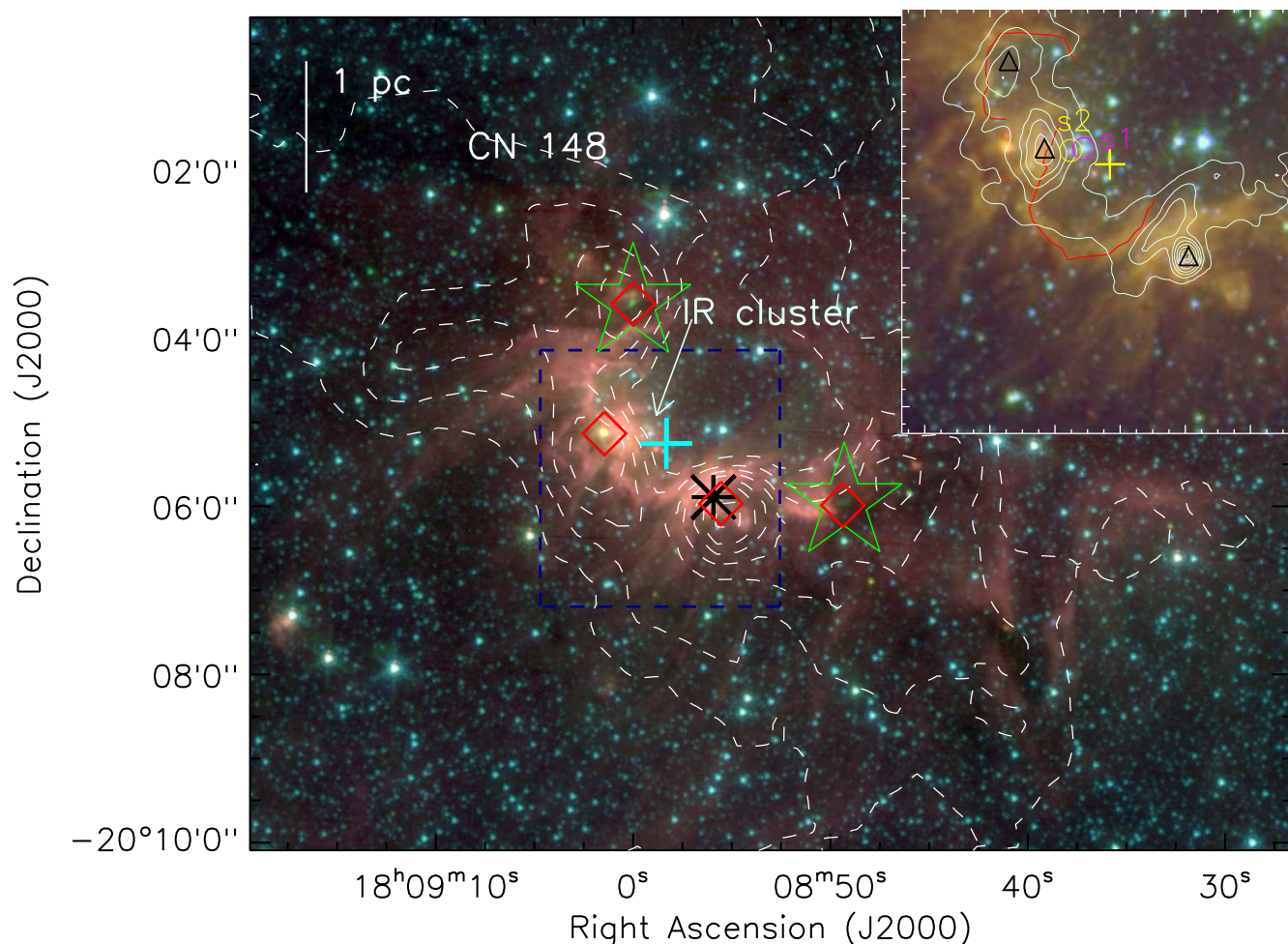


Figure 3. *Spitzer*-IRAC 8.0 μm (red), 4.5 μm (green), and 3.6 μm (blue) images in log scale from *Spitzer*-GLIMPSE survey. The dashed contours are integrated $^{13}\text{CO}(2-1)$ molecular gas emission from Beuther et al. (2011) with 10, 20, 30, 40, 55, 70, and 95% of the peak value i.e. 153.26 K km s $^{-1}$. The positions of IRAS 18060-2005 (+), four methanol masers (\diamond), water maser (big asterisk) and two EGOs (big star symbols) are marked in the figure. The inset on the top right represents the central region in zoomed-in view, made of *Spitzer*-IRAC 5.8 μm (red), 3.6 μm (green) and UKIDSS *K* (blue) images (see the blue dashed box in the main figure). MAGPIS 20 cm radio continuum contours are also shown on the inset image with similar levels to those as shown in Figure 2. Two arc-like structures, three 6 cm radio detections (\triangle) and IRAS 18060-2005 (+) are also drawn in the inset image. Two O-type candidates (s1 (18060nr1733) and s2 (18060nr2481)) visible in the inset image are shown by circle symbols.

Casali M., Adamson A., Alves de Oliveira C., Almaini O., Burch K., Chuter T., Elliot J., et al., 2007, *A&A*, 467, 777
 Casertano S., Hut P., 1985, *ApJ*, 298, 80
 Casoli F., Dupraz C., Gerin M., Combes F., Boulanger F., 1986, *A&A*, 169, 281
 Chambers E. T., Jackson J. M., Rathborne J. M., Simon R., 2009, *ApJS*, 181, 2
 Chavarría L. A., Allen L. E., Hora J. L., Brunt C. M., Fazio G. G., 2008, *ApJ*, 682, 445
 Churchwell E., Watson D. F., Povich M. S., et al., 2007, *ApJ*, 670, 428
 Churchwell E., 2008, *ASPC*, 390, 63
 Churchwell E., Babler B. L., Meade M. R., et al., 2009, *PASP*, 121, 213
 Contreras Y., Schuller F., Urquhart J. S., et al., 2013, *A&A*, 549, 45
 Corbel S., Wallyn P., Dame T. M., et al., 1997, *ApJ*, 478, 624

Cyganowski C. J., et al., 2008, *AJ*, 136, 2391
 Cyganowski C. J., Brogan C. L., Hunter T. R., Churchwell E., 2009, *ApJ*, 702, 1615
 Cyganowski C. J., Brogan C. L., Hunter T. R., Churchwell E., 2011, *ApJ*, 743, 56
 Deharveng L., Schuller F., Anderson L. D. et al., 2010, *A&A*, 523, 6
 Dewangan L. K., Anandarao B. G., 2011, *MNRAS*, 414, 1526
 Dewangan L. K., Ojha D. K., Anandarao B. G., Ghosh S. K., Chakraborti S., 2012, *ApJ*, 756, 151
 Dewangan L. K., Ojha D. K., 2013, *MNRAS*, 429, 1386
 Downes D., Wilson T. L., Bieging J., Wink J., 1980, *A&AS*, 40, 379
 Dye S., Warren S. J., Hambly N. C., Cross N. J. G., Hodgkin S. T., Irwin M. J., Lawrence A., et al., 2006, *MNRAS*, 372, 1227
 Dyson, J. E. and Williams, D. A. 1997, *Physics of the inter-*

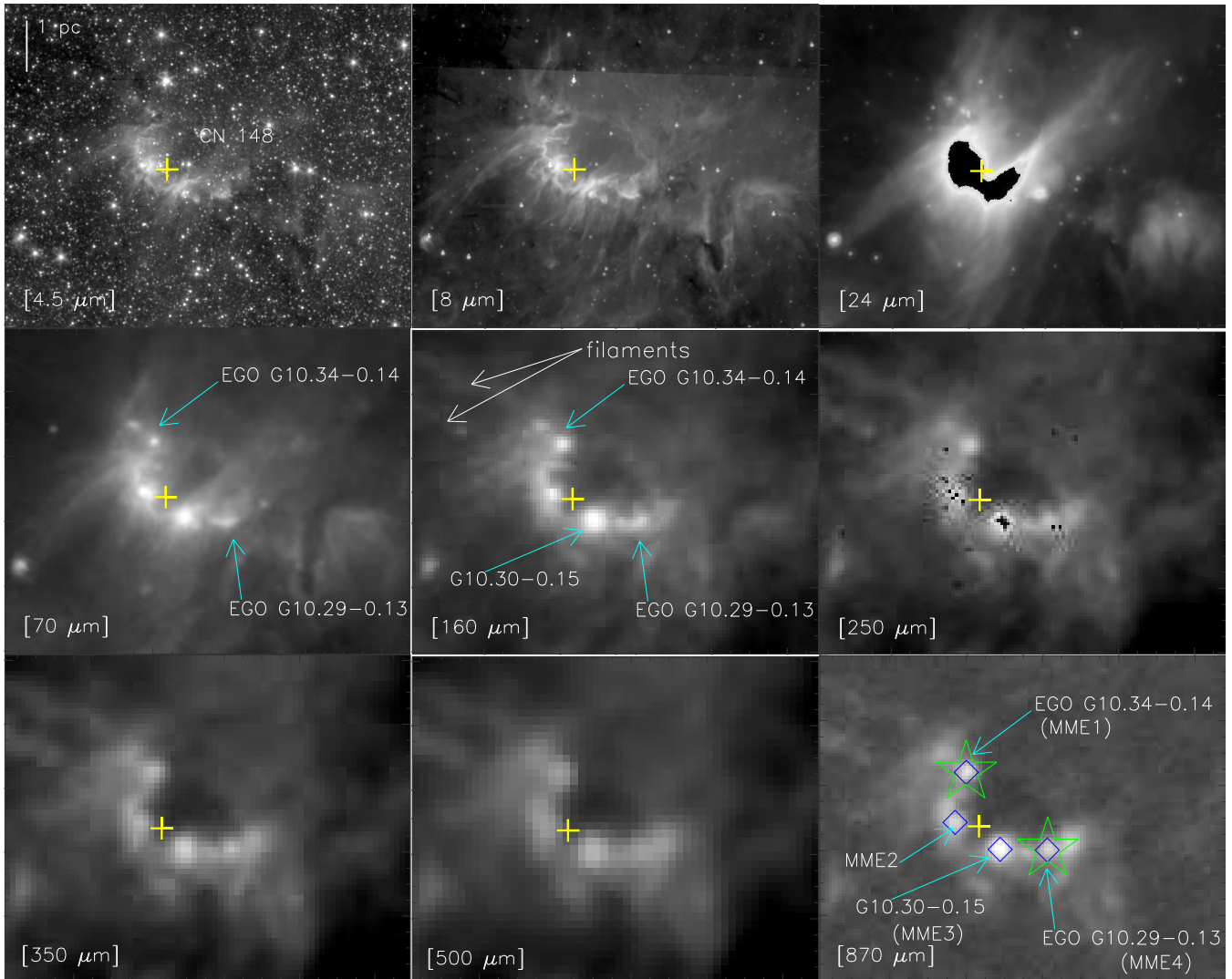


Figure 4. A multi-wavelength view around the bubble CN 148. The panels show images at 4.5 μm , 8.0 μm , 24 μm , 70 μm , 160 μm , 250 μm , 350 μm , 500 μm , 870 μm , from GLIMPSE, MIPS GAL, Hi-GAL, and ATLASGAL (from left to right in increasing order). The position of IRAS 18060-2005 is marked by a plus (+) symbol. The scale bar on the top left shows a size of 1 pc at a distance of 2.2 kpc. The 24 μm image is saturated near the IRAS position. Black dots seen at the 250 μm map can be an artifact. The 6.7 GHz methanol masers are also labeled as MME1-4 on 870 μm map. The other marked symbols are similar to those shown in Figure 3 (see the text for more details).

stellar medium, second edition, Institute of Physics publishing, Bristol and Philadelphia, 1997

Evans N. J., II, Dunham M. M., Jørgensen J. K., et al., 2009, *ApJS*, 181, 321

Fazio G. G., Hora J. L., Allen L. E., et al., 2004, *ApJS*, 154, 10

Flaherty K. M., Pipher J. L., Megeath S. T., Winston E. M., Gutermuth R. A., Muzerolle J., Allen L. E., Fazio, G. G., 2007, *ApJ*, 663, 1069

Froebrich D., Davis C. J., Ioannidis G., et al., 2011, *MNRAS*, 413, 480

Getman K. V., Feigelson E. D., Garmire G., Broos P., Wang J., 2007, *ApJ*, 654, 316

Ghosh S. K., Iyengar K. V. K., Rengarajan T. N., et al., 1989, *ApJ*, 347, 338

Gutermuth R. A., Megeath S. T., Myers P. C., Allen L. E., Pipher J. L., Fazio G. G., 2009, *ApJS*, 184, 18

Hartmann L., Megeath S. T., Allen L., Luhman K., Calvet N., D'Alessio Paola, Franco-Hernandez R., Fazio G., 2005, *ApJ*, 629, 881

Helfand D. J., Becker R. H., White R. L., Fallon A., Tuttle S., 2006, *AJ*, 131, 2525

Helou G., Walker D. W., 1988, *IRAS*, 7

Hildebrand R. H., 1983, *Quarterly Journal of the RAS*, 24, 267

Hodgkin S. T., Irwin M. J., Hewett P. C., Warren S. J., 2009, *MNRAS*, 394, 675

Indebetouw R., Mathis J. S., Babler B. L., et al., 2005, *ApJ*, 619, 931

Kendrew S., Simpson R., Bressert E., et al., 2012, *ApJ*, 755, 71

Kim K. T., Koo B. C 2001, *ApJ*, 549, 979

Kim K. T., Koo B. C 2002, *ApJ*, 575, 327

Kudritzki R. -P., Puls J., 2000, *ARA&A*, 38, 613

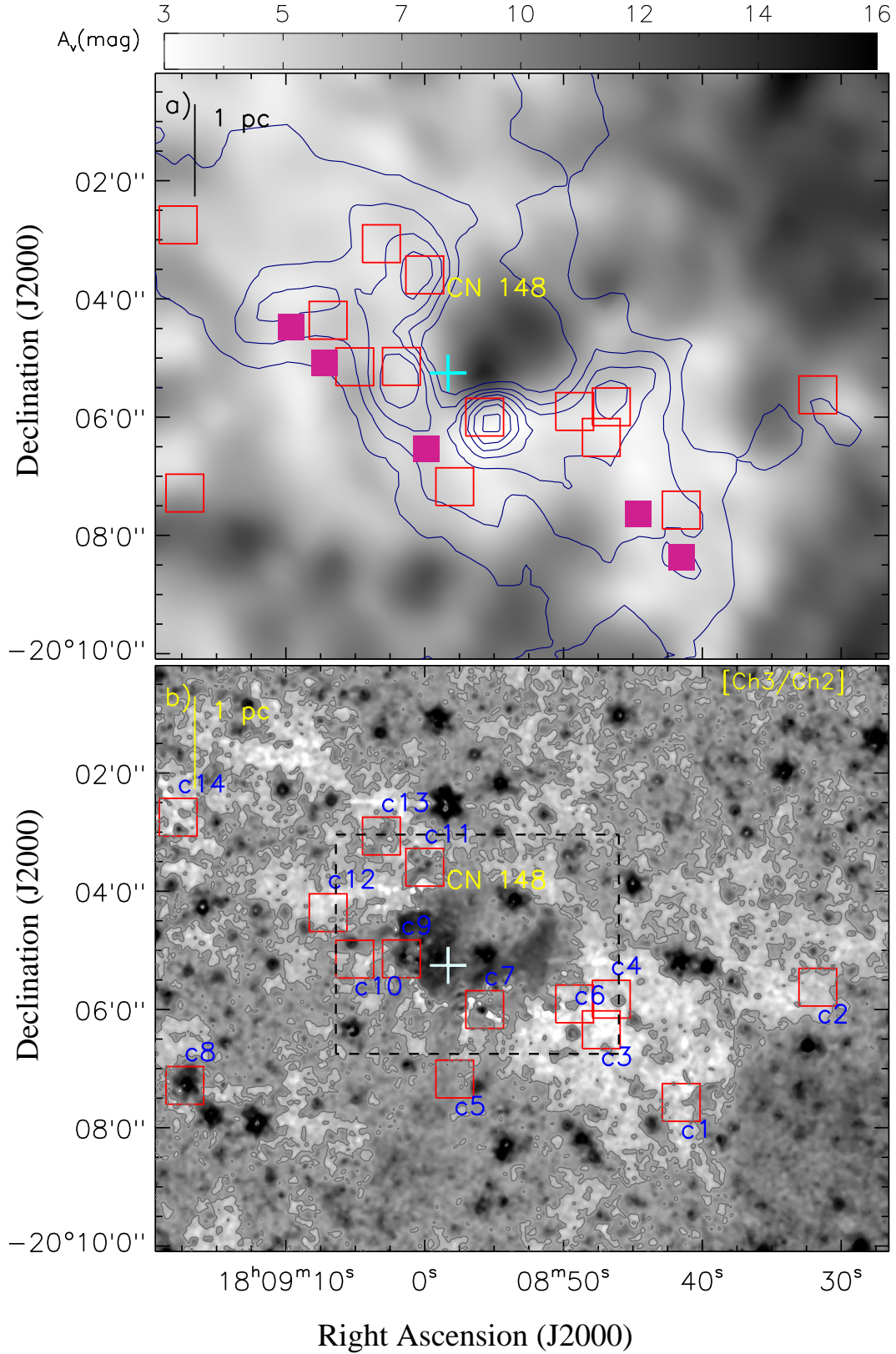


Figure 5. a) Visual extinction (A_V) map of the region obtained using NIR data (see text for details). Integrated molecular $^{13}\text{CO}(2-1)$ emission is overlaid with navy blue contours similar to those as shown in Figure 3. The peak positions of five starless clumps (Tackenberg et al. 2012) are also marked by filled square symbols. b) *Spitzer*-IRAC ch3/ch2 ratio map around CN 148 (for a similar area as in Figure 2). The ch3/ch2 ratio contours are also shown on the image with a representative value of 8.3. The black dashed box is shown as a zoomed-in view in Figure 6. The positions of dust clumps are marked by big red square symbols in both images and labeled in Figure 5b (see Table 2). Other marked symbols are the same as in Figure 3.

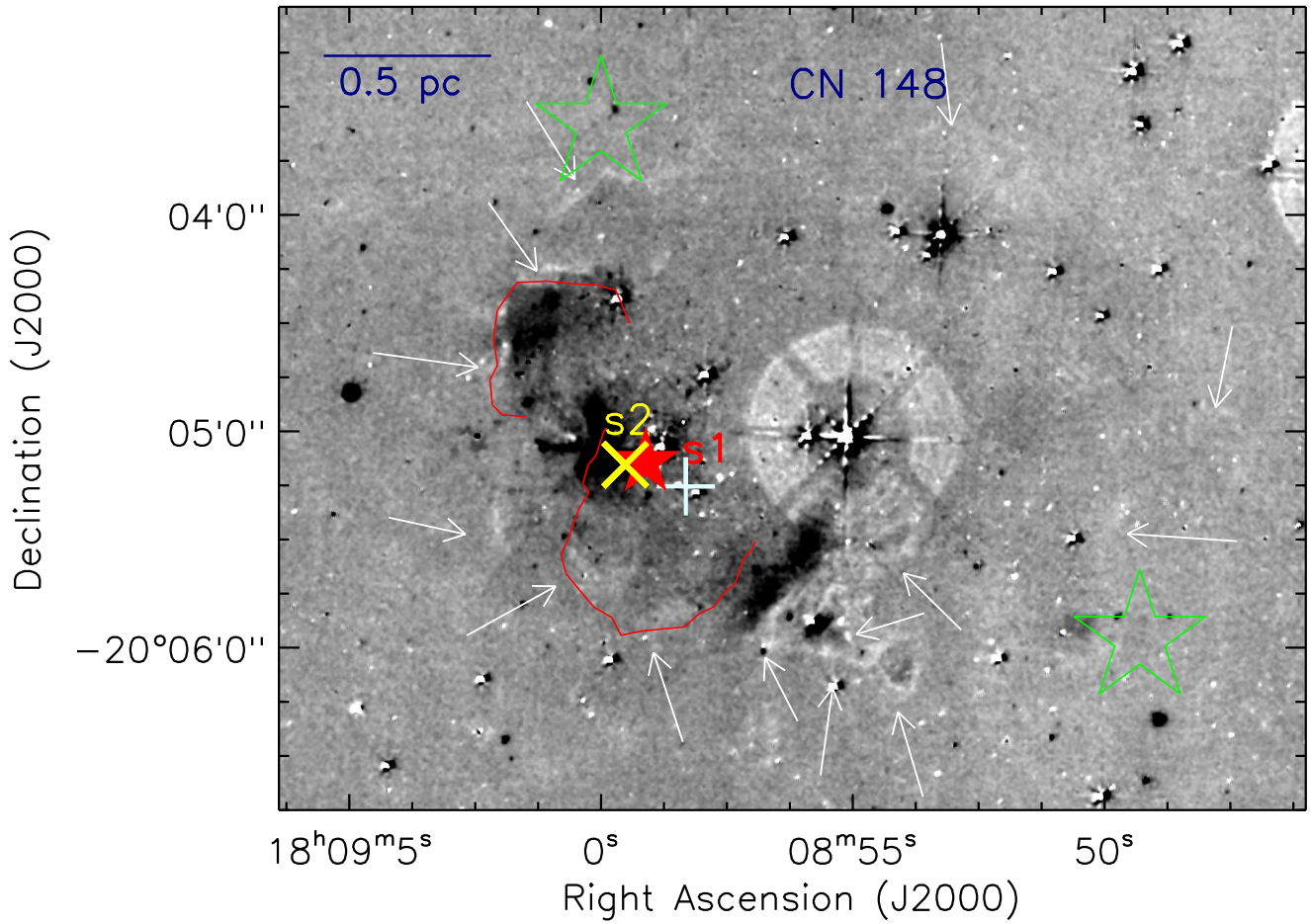


Figure 6. Map of continuum-subtracted H₂ image (gray-scale) at 2.12 μm around CN 148 (size of selected region in map $\sim 4.8 \times 3.7$ arcmin²; as shown by a dashed box in Figure 5b). White arrows indicate the detected H₂ emission along the bubble (as seen in GLIMPSE images). The marked symbols are similar to those shown in Figures 2 and 3. Two red arc-like curves are similar as shown in Figure 3. The final continuum-subtracted H₂ image was obtained from UWISH2 survey (Froebrich et al. 2011) and was further processed through median filtering with a width of 5 pixels and smoothed by 4 pix \times 4 pix using a boxcar algorithm to trace the faint features in the image.

Kumar M. S. N., Davis C. J., Grave J. M. C., Ferreira B., Froebrich D., 2007, MNRAS, 374, 54
 Kwan J., 1997, ApJ, 489, 284
 Lada C. J., et al. 2006, AJ, 131, 1574
 Lawrence A., Warren S. J., Almaini O., et al. 2007, MNRAS, 379, 1599
 Lombardi M., Alves J., 2001, A&A, 377, 1023
 Lucas P. W., Hoare M. G., Longmore A., Schröder A. C., Davis C. J., Adamson A., Bandyopadhyay R. M., de Grijs R., et al., 2008, MNRAS, 391, 1281
 Lumsden S. L., Hoare M. G., Urquhart J. S., et al., 2013, ApJS, 208, 11
 Martins F., Schaerer D., Hillier D. J., 2005, A&A, 436, 1049
 Matsakis D. N., Evans N. J., II, Sato T., Zuckerman B., 1976, AJ, 81, 172
 Moisés A. P., Damineli A., Figuerêdo E., Blum R. D., Conti P. S., Barbosa C. L., 2011, MNRAS, 411, 705
 Molinari S., Swinyard B., Bally J., et al. 2010, A&A, 518, L100
 Ott S., 2010, in Astronomical Society of the Pacific Conference Series, Vol. 434, Astronomical Data Analysis Soft-

ware and Systems XIX, ed. Y. Mizumoto, K.-I. Morita, & M. Ohishi, 139
 Paladini R., Umana G., Veneziani M., et al., 2012, ApJ, 760, 149
 Panagia N. 1973, AJ, 78, 928
 Panagia N., Walmsey C. M., 1978, A&A, 70, 711.
 Povich M. S., Stone J. M., Churchwell E., et al., 2007, ApJ, 660, 346
 Reich W., Reich P., Fürst, E., 1990, A&AS, 83, 539
 Rieke G. H., Lebofsky M. J., 1985, ApJ, 288, 618
 Robitaille T. P., Whitney B. A., Indebetouw R., Wood K., Denzmore P., 2006, ApJS, 167, 256
 Robitaille T. P., Whitney B. A., Indebetouw R., Wood K., 2007, ApJS, 169, 328
 Robitaille T. P., Meade M. R., Babler B. L., et al., 2008, AJ, 136, 2413
 Schuller F., Menten K. M., Contreras Y., et al., 2009, A&A, 504, 415
 Skrutskie M. F., Cutri R. M., Stiening R., Weinberg M. D., Schneider S., Carpenter J. M., Beichman C., et al., 2006, AJ, 131, 1163

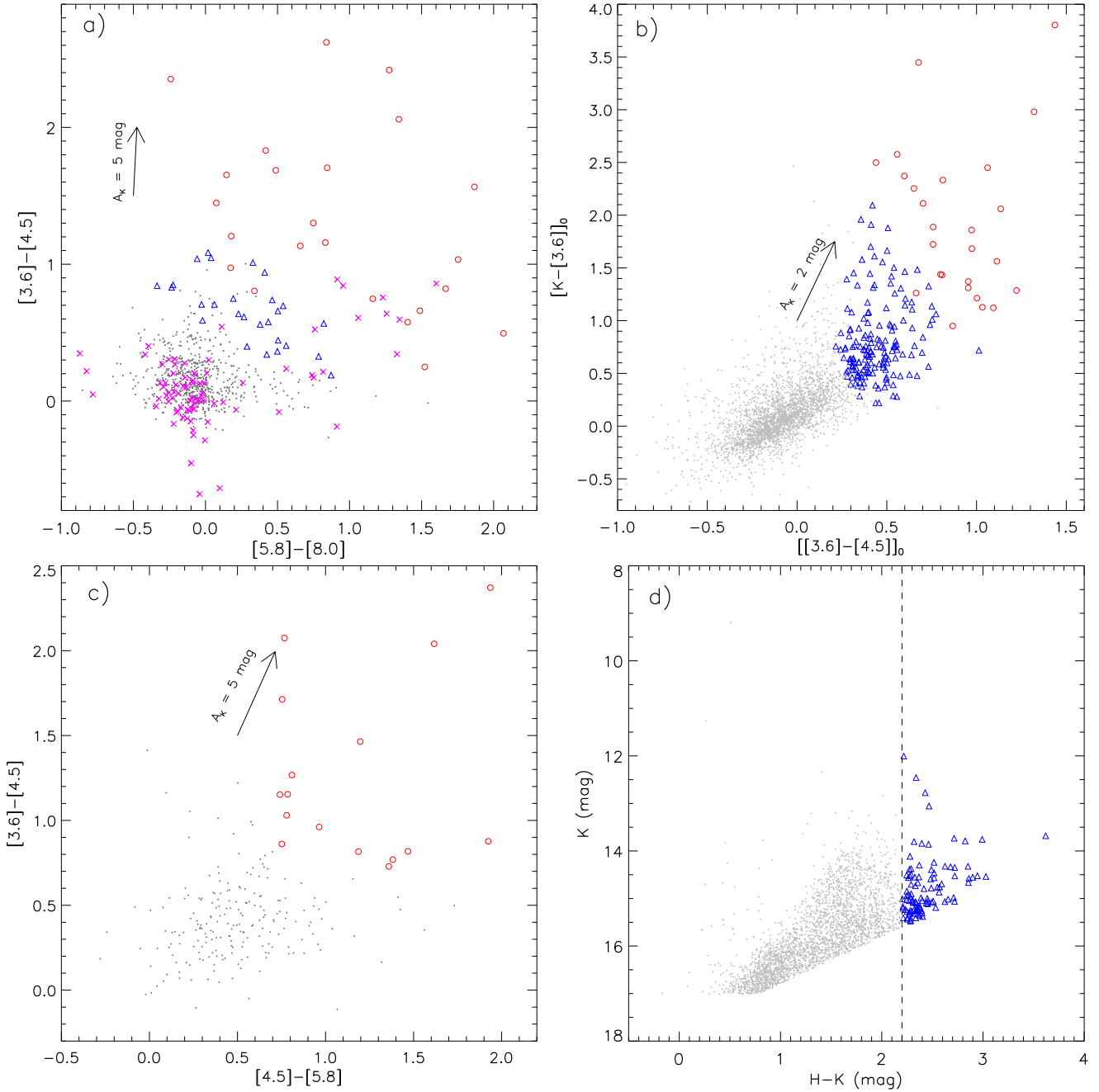


Figure 7. Color-color and color-magnitude diagrams for all the sources identified within the region shown in Figure 2. a) Color-color diagram ($[3.6]-[4.5]$ vs. $[5.8]-[8.0]$) using *Spitzer*-IRAC four band detections. The arrow shows the extinction vector with $A_K = 5$ mag using the average extinction law from Flaherty et al. (2007). The dots in gray color represent the stars with only photospheric emissions. The Class 0/I and Class II YSOs are shown by open red circles and open blue triangles, respectively. The “x” symbols in magenta color show the identified PAH-emission-contaminated apertures in the region (see the text). b) The dereddened $[K - [3.6]]_0$ vs $[[3.6] - [4.5]]_0$ color-color diagram using NIR and GLIMPSE data. The arrow represents the extinction vector with $A_K = 2$ mag using the average extinction law from Flaherty et al. (2007). Open red circles and open blue triangles show Class I and Class II sources, respectively. c) Color-color diagram ($[3.6]-[4.5]$ vs. $[4.5]-[5.8]$) of the sources detected in three IRAC bands, except $8.0 \mu\text{m}$. The protostars are marked by open red circles (see the text for YSOs selection criteria). The arrow shows the extinction vector with $A_K = 5$ mag using the average extinction law from Flaherty et al. (2007). d) Color-magnitude diagram ($K/H-K$) of the sources detected only in H and K bands. The YSOs are marked by open blue triangles (see the text for YSOs selection criteria).

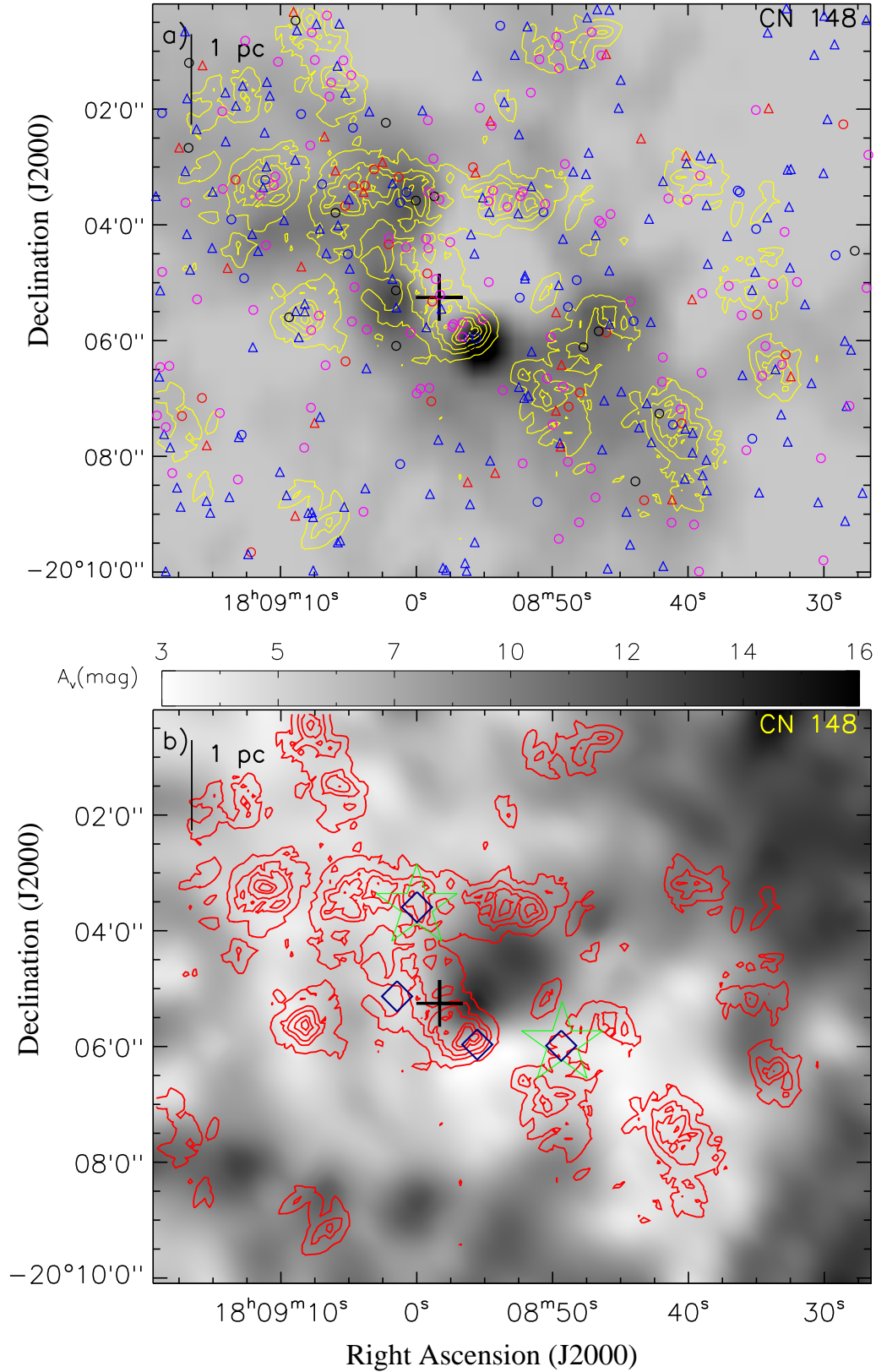


Figure 8. a) The spatial distribution of YSOs and molecular $^{13}\text{CO}(2-1)$ gas emission in the selected region around CN 148. The YSO surface density contours are drawn in yellow color for 10, 15, 20, 30, and 40 YSOs/pc², from the outer to the inner side (see text for details). The open circles and open triangles show the Class I and Class II sources, respectively. The YSOs identified using four IRAC bands, WFCAM-IRAC, three IRAC bands and red sources ($H-K > 2.2$) are shown by red, black, blue, and magenta colors, respectively. The position of IRAS 18060-2005 (+) is also marked in the plot. b) The YSO surface density contours are drawn in red color similar levels to as shown in Figure 8a, and are superimposed on the visual extinction map. Other marked symbols are the same as in Figure 3.

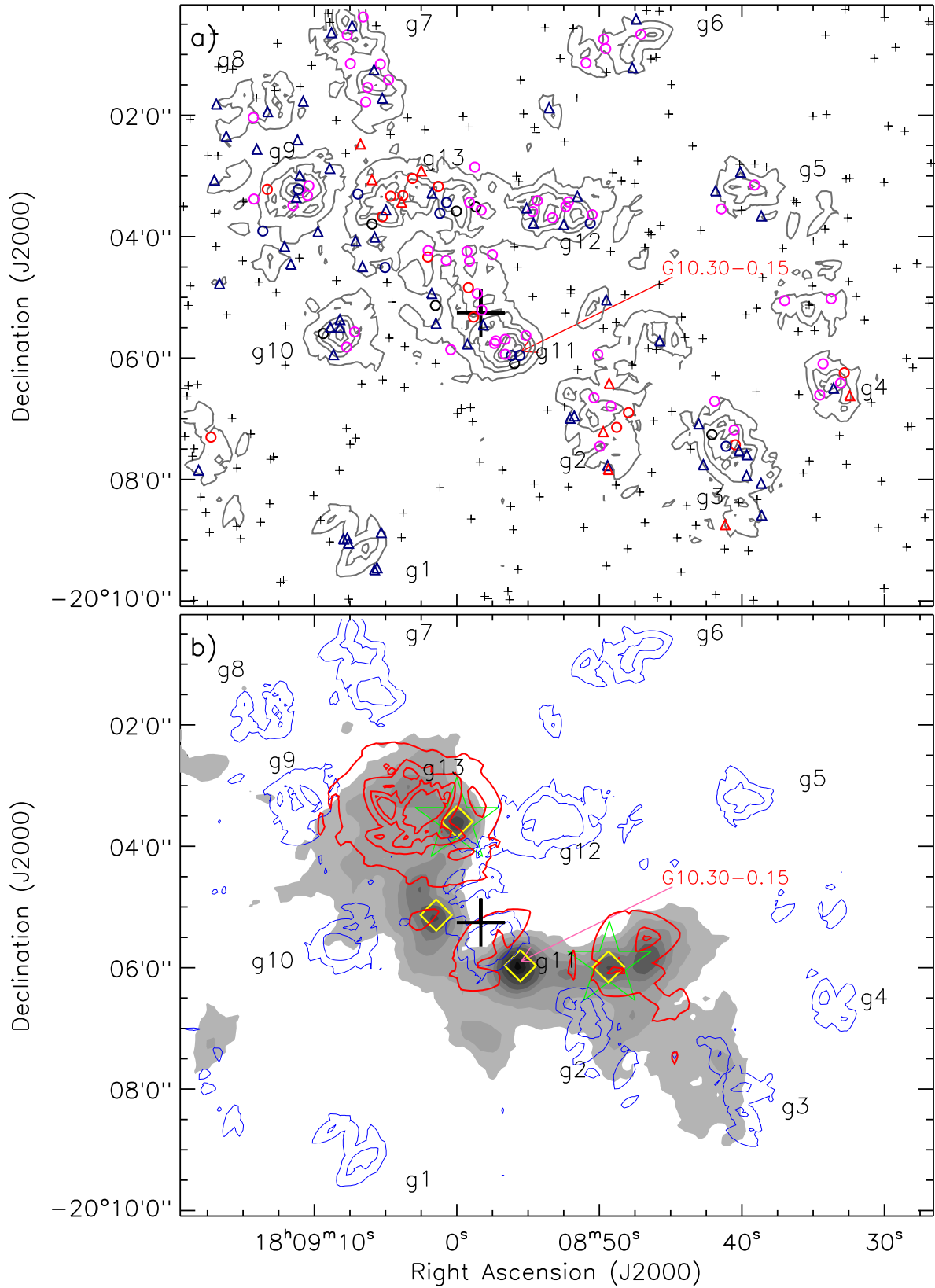


Figure 9. a) All the selected cluster YSO members with $d_c \lesssim 0.47$ pc are shown by open circles (Class I) and open triangles (Class II). The YSOs greater than d_c ($= 0.47$ pc) are marked by plus symbols (black) (see text for details). The identified clusters are labeled in the diagram (see Table 3). The other marked symbols are similar to those shown in Figure 8a. b) Comparison between the surface density contour maps of Class I and Class II YSOs in the selected region around the bubble CN 148. The surface density contours of Class I YSOs are drawn in red color with 3.5, 6, 8, and 10 YSOs/ pc^2 . The Class II YSO surface density contours are overlaid in blue color with 10 and 15 YSOs/ pc^2 . The background gray area indicates the contour map of ATLASGAL 870 μm emissions with 5, 10, 20, 30, 40, 55, 70, 85, and 95% of the peak value i.e. 7.57 Jy/beam. The other marked symbols are similar to those shown in Figures 3 and 9a.

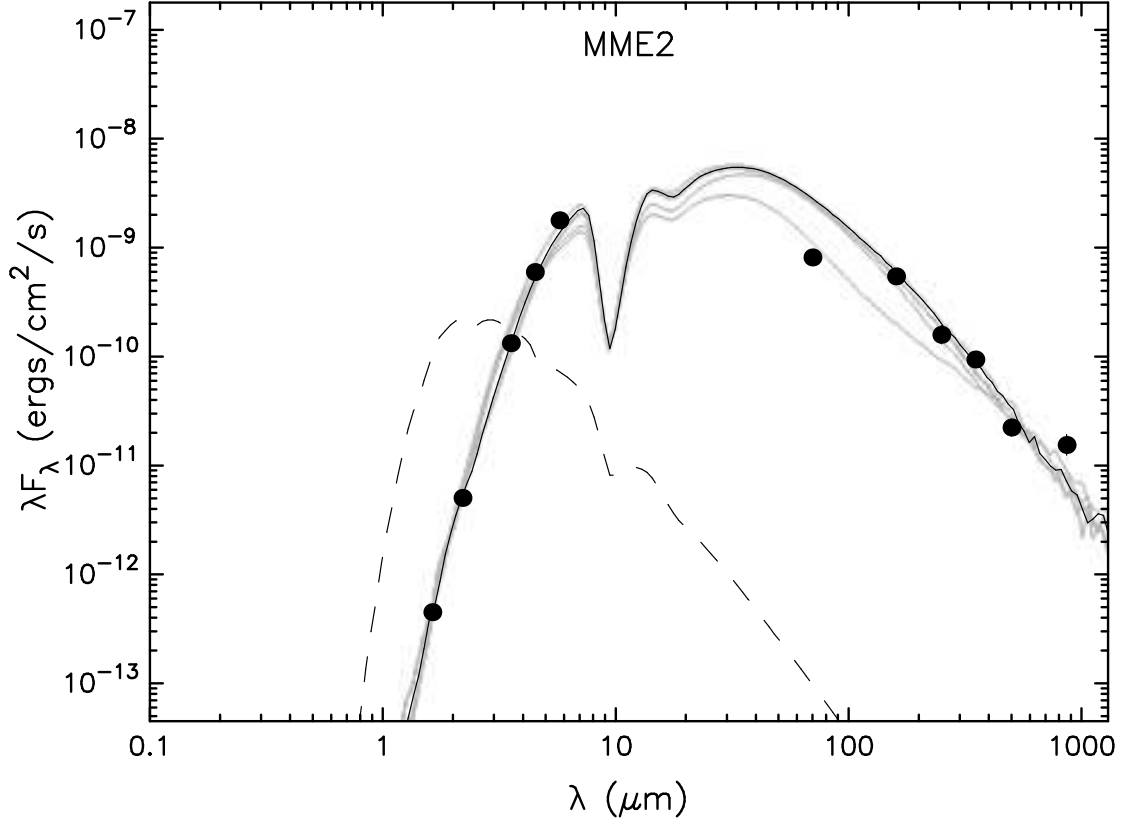


Figure 10. The SED plot of the IRC of the maser MME2. The filled circles are observed fluxes of good quality (see Section 3.2.4) and the grey curves show the fitted model for $(\chi^2 - \chi^2_{best})$ per data point < 5 . The thin black curve corresponds to the best fitting model. The dashed curves represent photospheric contributions.

- Tackenberg J., Beuther H., Henning T., Schuller F. et al., 2012, *A&A*, 540, 112
 Thompson M. A., Urquhart J. S., Moore T. J. T., Morgan L. K., 2012, *MNRAS*, 421, 408
 Tielens A. G. G. M., Peeters E., Bakes E. L. O., Spoon H. W. W., Hony S., 2004, *ASPC*, 323, 135
 Veneziani M., Elia D., Noriega-Crespo A., et al., 2013, *A&A*, 549, 130
 Vink J. S., de Koter A., Lamers H. J. G. L. M., 2001, *A&A*, 369, 574
 Walsh A. J., Burton M. G., Hyland A. R., Robinson G., 1998, *MNRAS*, 301, 640
 Whitney B. A., Sewilo M., Indebetouw R., et al., 2008, *AJ*, 136, 18
 Wienen M., Wyrowski F., Schuller F., Menten K. M., Walmsley C. M., Bronfman L., Motte F., 2012, *A&A*, 544, 146
 Wilson T. L., 1974, *A&A*, 31, 832
 Wood D. O. S., Churchwell E., 1989, *ApJS*, 69, 831
 Wright E. L., Eisenhardt P. R. M., Mainzer A. K., Ressler M. E., et al., 2010, *AJ*, 140, 1868